ORIGINAL ARTICLE

lajss.org Latin American Journal of Solids and Structures

www.lajss.org

Mechanical Properties of Silicon Carbide Ceramic and Its Penetration Resistance to Tungsten Alloy Fragments

Dacheng Gao[a], Guixiang Yin[b], Kebin Zhang[c], Yiming Li[a], Wenbin Li[a]*

[a] School of Mechanical Engineering, Nanjing University of Science and Technology, Nanjing 210094, China. Email: gaodacheng001@163.com, Liyiming0919@163.com, lwb2000cn@njust.edu.cn.
[b] No.52 Institute of China Ordnance Industries, Yantai 264003, China. Email: dzsygx@163.com.
[c] School of Mechatronics Engineering, North University of China, Taiyuan 030051, Shanxi, China. Email: 20230206@nuc.edu.cn.

* Corresponding author

https://doi.org/10.1590/1679-7825/e9203

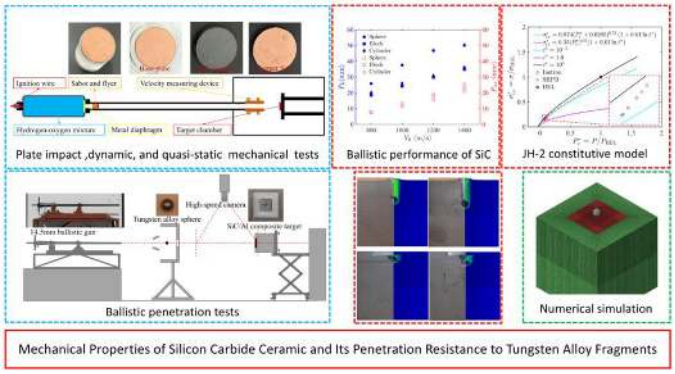
Abstract

Silicon carbide (SiC) ceramics have been widely used in lightweight armor protection due to their combination of high compressive strength, high hardness, and low density. The mechanical properties and penetration resistance of SiC ceramics are of significant importance for armor protection design. To investigate the mechanical response and fragment penetration resistance of SiC ceramics, this study systematically carried out plate impact tests, dynamic and quasi-static uniaxial compression tests, as well as ballistic penetration tests. Based on the experimental data, the parameters of the Johnson-Holmquist II (JH-2) constitutive model for the SiC ceramic were calibrated. Subsequently, a numerical simulation model of tungsten alloy fragment penetration into SiC ceramic composite targets was established. The model was validated using tungsten alloy fragment penetration tests on SiC/6061-T6 composite targets, and the penetration characteristics of fragments into SiC/6061-T6 composite targets were systematically compared with those into monolithic 6061-T6 aluminum alloy targets. The error between the experimental and simulation results of the composite target penetration tests is less than 9%, verifying the accuracy of the calibrated JH-2 model parameters. For monolithic 6061-T6 aluminum alloy targets, the penetration depth of spherical fragments is significantly greater than that of cubic and cylindrical fragments. In contrast, for the ceramic composite targets, the residual penetration depth of spherical fragments is markedly lower, indicating that SiC ceramic exhibits substantially better resistance to spherical fragments than to the other two fragment shapes. This study can provide a theoretical basis and data support for the design and performance evaluation of lightweight armor protection.

Keywords

armor protection; silicon carbide ceramics; JH-2 constitutive model; ballistic impact; numerical simulation; tungsten alloy fragment

Graphical Abstract



Received July 17, 2026. In revised form August 20, 2026. Accepted August 26, 2026. Available online August 28, 2026.
https://doi.org/10.1590/1679-7825/e9203

Latin American Journal of Solids and Structures. ISSN 1679-7825. Copyright © 2026. This is an Open Access article distributed under the terms of the Creative Commons Attribution License, which permits unrestricted use, distribution, and reproduction in any medium, provided the original work is properly cited.

1 INTRODUCTION

Silicon carbide (SiC) ceramics exhibit excellent ballistic performance due to their low density and high strength, leading to their increasingly widespread application in armor protection. A comprehensive understanding of the mechanical behavior, constitutive model and penetration resistance of these materials is therefore critically important for the rational design and reliable assessment of military equipment and ballistic protection systems (Zhai et al. 1963, Sun et al. 2025, Iqbal et al. 2024, Wu et al. 2023, Yu et al. 2021).

Under intense dynamic loading conditions such as ballistic impact, the dynamic mechanical behavior of ceramics serves as the theoretical foundation for evaluating their penetration resistance. Accordingly, researchers worldwide have conducted systematic experimental studies on typical ceramics, including SiC. Feng et al. (1998) performed compressive and shear wave measurements on SiC fabricated by three different processes using plate impact tests. The results revealed that its Hugoniot elastic limit (HEL) was approximately 11.5 GPa. The maximum shear stress increased from 4.5 GPa to 6.4 GPa under a peak stress of 18 GPa, indicating a shock-hardening effect. In addition, plate impact tests under uniaxial strain have provided critical data for understanding the inelastic deformation of the material and for calibrating constitutive models (Holmquist et al. 2002). Zhang et al. conducted quasi-static and dynamic compression tests on 6H-SiC and found that under quasi-static loading (strain rate of 10^{-5}–10^{-3} s^{-1}), SiC exhibited purely brittle fracture, whereas under dynamic SHPB compression (specimen dimensions: 6×6×4 mm^3), plastic deformation occurred (Zhang et al. 2018). Gao (2014) performed SHPB experiments on alumina, SiC, and Al_2O_3/SiC composite ceramics, and observed that layered cracks, intergranular cracks, and transgranular cracks were the dominant crack types under high strain rate compression.

In the study of the penetration resistance of ceramics, numerical simulation has been widely adopted, often in combination with ballistic tests, to reduce cost and improve efficiency. However, the accuracy of numerical simulations largely depends on the dynamic constitutive model of the ceramic material. To address this, researchers have proposed various models (Rajendran 1994, Johnson 1993, Simha et al.2002, Ravichandran 1995, Espinosa 1995, Espinosa et.al 2005, Steinberg 1992). For ballistic impact problems, Rajendran (1994) assumed an initial distribution of microcracks and adopted a crack propagation criterion based on dynamic fracture mechanics theory to simulate the impact behavior of AD85 ceramic under multiaxial loading. The early Johnson-Holmquist I (JH-1) model (Johnson et al. 1992, Quan 2006) considered factors such as pressure-dependent damage and cracking, post-cracking effective strength, volumetric change, and strain-rate effects, but it did not account for the damage evolution process. To overcome this limitation, the Johnson-Holmquist II (JH-2) model was subsequently developed (Johnson 1999).

The JH-2 constitutive model introduces a continuous damage evolution variable, enabling it to describe the strength softening process of ceramic materials from an intact state through progressive damage to complete failure, rather than the simple “intact-failure” binary state in the JH-1 model. The JH-2 model more realistically captures the damage accumulation and dynamic response of materials under impact loading, and has been widely adopted in numerical simulations of ceramic penetration resistance. Yin et al. (2010) fabricated an Al_2O_3-based composite ceramic, systematically investigated its mechanical properties, and ultimately calibrated the JH-2 constitutive model parameters. Yang et al. (2010) obtained the JH-2 constitutive parameters for alumina ceramics by combining existing literature data with experimental and numerical simulation methods. Based on this damage-dependent dynamic constitutive model, numerical simulations of the fragmentation process of alumina ceramics under low-velocity impact were performed using the LS-DYNA explicit finite element software, successfully reproducing the damage evolution and dynamic fragmentation behavior of the specimens. Holmquist et al. (2001) determined the JH-2 constitutive parameters for aluminum nitride (AlN) under high-velocity impact using available data from mechanical tests and ballistic tests; these model parameters yielded reasonable results in subsequent numerical simulations. An et al. (2023) proposed a method for obtaining and optimizing the key parameters of the JH-2 model for brittle materials, and analyzed the sensitivity of damage-related parameters in dynamic compression tests and penetration processes. In the following year, An et al. (2024) employed machine learning and numerical simulations to investigate the relationship between the physical properties and ballistic performance of ceramics. The study found that density, dynamic compressive strength, quasi-static compressive strength, and HEL have the most significant influence on the residual penetration depth. Drawing on studies of concrete, Tang et al. (2020) proposed a macroscopic constitutive model for ceramic materials under dynamic loading. The equation of state was represented by a polynomial, while the strength model incorporated multiple mechanisms, including pressure hardening, strain rate effects, shear damage, and tensile softening.

Relatively few studies have focused on the resistance of ceramics to fragment penetration. Jiang et al. (2001) conducted ballistic tests on the normal penetration of tungsten alloy spheres into ceramic/aluminum composite targets, revealing the interaction process between the tungsten alloy sphere and the target, and analyzing the penetration resistance mechanism of the ceramic/aluminum composite target. Li et al. (2002) developed an analytical model for the ballistic limit of the tungsten

sphere penetrating a ceramic composite target by analyzing the backplate deformation from an energy perspective based on experimental results. Mao et al. (2015) studied the normal impact of tungsten alloy spherical fragments on ceramic/DFRP composite targets with different thickness ratios using a ballistic gun dynamic loading device. They obtained the relationship between the ballistic limit velocity (v_{50}) and the areal density (AD) of the composite targets, and established an empirical formula for v50 based on dimensional analysis, which agreed well with the experimental results.

To systematically investigate the JH-2 constitutive model of the SiC ceramic and its penetration resistance, this study comprehensively integrated mechanical property tests, numerical simulation analysis, and ballistic test validation. Regarding the mechanical property tests, the HEL of the SiC ceramic was measured through plate impact tests (plane wave loading), and the damage evolution parameters were calibrated. Quasi-static compression and split Hopkinson pressure bar (SHPB) dynamic compression tests were employed to obtain the strength parameters of the intact material and the strain rate effect parameters in the JH-2 constitutive model. Using the calibrated constitutive model parameters, the penetration resistance of SiC ceramic target plates subjected to high-velocity impact by tungsten alloy fragments of three different shapes was systematically analyzed using numerical simulation methods and the ABAQUS/Explicit finite element software. Finally, the accuracy of the established constitutive model and the validity of the numerical simulation were verified by comparing with ballistic test results, providing a reliable predictive tool for the application of SiC ceramics in protective structures.

2 MECHANICAL PROPERTY TESTS

Accurately calibrating the JH-2 constitutive model parameters for the ceramic material requires a series of mechanical tests that account for its strength and pressure response under various strain rates and stress states. Plate impact tests were used to determine the HEL of the SiC ceramic under one-dimensional strain loading. The HEL served as the reference for stress normalization in the JH-2 model. These tests also assisted in calibrating the damage evolution parameters. Quasi-static compression tests provided the static compressive strength at low strain rates, while dynamic compression tests (e.g., SHPB) revealed the dynamic strength and strain-rate sensitivity of the material at intermediate to high strain rates (10^2–10^4 s^{-1}). Combined with the static compressive strength, the dynamic test results allowed calibration of the strain-rate coefficients in the JH-2 model. The key parameters of the JH-2 constitutive model were fully calibrated based on the above experimental data.

2.1 Specimen preparation

The SiC ceramic used in this study was fabricated via a pressureless sintering process. Pressureless sintering refers to a high-temperature densification process in which powder diffusion and compaction are driven solely by thermal activation under ambient pressure without applying external mechanical pressure. This method offers advantages including relatively simple equipment requirements, low cost, and the capability to produce large-scale or geometrically complex ceramic components. Moreover, it yields ceramics with a relative density approaching theoretical values (typically 95%–99%), along with fine grains and a homogeneous microstructure. First, SiC micropowder (average particle size of 5 μm) was mixed with appropriate sintering additives (e.g., boron and carbon) at a predetermined ratio. The mixture was subjected to ball milling or attrition milling to obtain a uniformly dispersed slurry, which was subsequently spray-dried to produce free-flowing granulated powder. The granulated powder was then compacted via cold isostatic pressing to form a dense, homogeneous green body. The green body was sintered in a high-temperature atmosphere furnace under argon protection at 2000 °C for a holding time of 2h. Then, the raw plates (50 mm × 50 mm × 6 mm) were obtained.

Due to the high hardness (HV ≈ 25–30 GPa) and high brittleness of SiC ceramics, conventional mechanical cutting tends to induce microcracks and edge chipping. Therefore, laser cutting was employed for precise trimming of the as-prepared bulk ceramic plates. Laser cutting offers advantages such as a narrow kerf, a small heat-affected zone (HAZ), and the absence of mechanical stress, thereby effectively avoiding processing-induced damage that could affect the results of mechanical tests. According to the specific requirements of the different mechanical tests, the ceramic plates were machined into the following three types of specimens:

1. Flyer impact specimens: For plate impact tests, discs of 18 mm in diameter and 3 mm in thickness were machined. The top and bottom surfaces of the specimens were precision ground and polished to a surface roughness Ra ≤ 0.8 μm, with a parallelism between the two planes ≤ 0.08 mm and a flatness ≤ 0.04 mm.
2. Quasi-static compression specimens: Cylindrical specimens with a diameter of 4 mm and a height of 5 mm (aspect ratio of 1.25) were machined. The perpendicularity error between the specimen end faces and the axis was ≤ 0.015 mm, parallelism between the top and bottom end faces ≤ 0.01 mm, and lateral surface roughness Rz ≤ 3.2 μm.

3. Dynamic compression (SHPB) specimens: To be compatible with split Hopkinson pressure bar tests, small cylinders of 4 mm in diameter and 3 mm in height (aspect ratio of 0.75) were machined. To reduce the influence of end-face friction on the stress-strain response at high strain rates, the end face roughness was required to be Ra ≤ 0.8 μm. Parallelism between the top and bottom surfaces was ≤ 0.01 mm, and perpendicularity ≤ 0.01 mm.

The basic material properties of the SiC ceramic are summarized in Table 1.

Table 1. Material properties of SiC ceramic.

Density	Longitudinal wave velocity	Shear wave velocity	Poisson's ratio	Young's modulus	Shear modulus	Bulk modulus	Tensile strength
$\rho_{0,c}$ (kg/m^3)	$V_{p,c}$ (m/s)	$V_{s,c}$ (m/s)	v	E (GPa)	G (GPa)	K_1 (GPa)	T_c (MPa)
3130	11765	7415	0.1705	403	172	204	260

2.2 Plate impact tests

The plate impact tests on ceramics were conducted using a single-stage hydrogen oxygen gun as the shock loading platform (as shown in Figure 1 and Figure 2). During the test, a predetermined amount of hydrogen and oxygen was filled into the reaction chamber. Upon ignition by an electrical wire, a hydrogen-oxygen detonation occurred, generating high-temperature and high-pressure gases that ruptured the metal diaphragm and propelled the sabot forward within the launch tube. The launch tube has an inner diameter of 30 mm and a length of 6 m. The sabot was accelerated and subsequently impacted the target plate to complete the shock loading process. The velocity of the projectile sabot at the muzzle was recorded by a magnetic velocity measurement system. The entire launching process was performed under a low-vacuum environment.

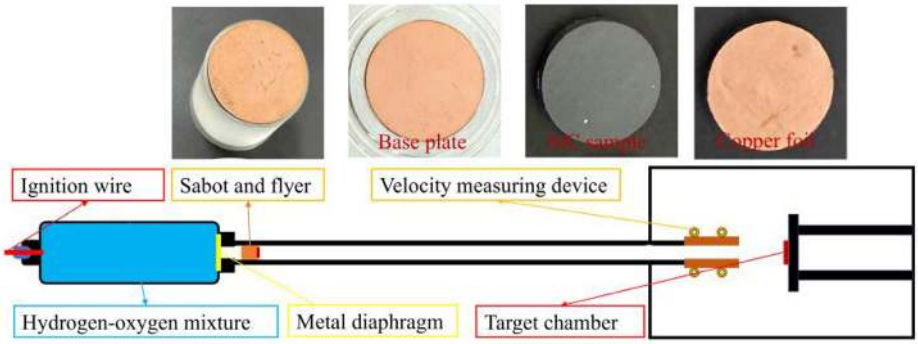


Figure 1 Schematic diagram of the single-stage hydrogen-oxygen gun structure.

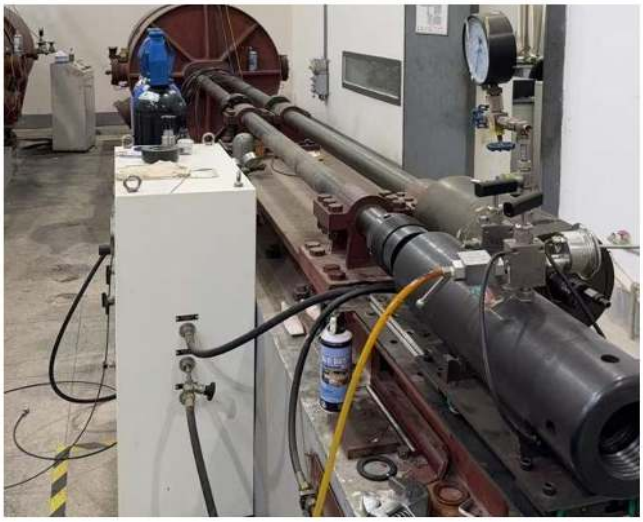


Figure 2 Photograph of the single-stage hydrogen-oxygen gun.

Plate impact tests on ceramics were conducted in a free-surface configuration. The velocity profile evolution at the rear free surface of the ceramic specimen was directly recorded to observe the elastic-plastic transition point and to measure the shock wave. To enhance the signal strength, a 25-μm-thick copper foil was attached to the free surface of the SiC sample to improve its reflectivity to the 1550 nm laser, thereby increasing the quality of the detected optical signal. Since the thickness of the copper foil (25 μm) is much smaller than that of the SiC specimen, the shock wave transit time through the copper layer is only about 5 ns, which falls within the temporal resolution of the VISAR system and is far shorter than the characteristic rise time of the measured wave profiles. Therefore, the wave impedance mismatch induced by the copper foil are negligible and do not affect the experimental results. The flyer material used in the tests was identical to that of the base plate. To achieve different impact pressures, SiC, Oxygen-free high-conductivity copper (OFHC), and tantalum (Ta) were selected as flyer materials. When the flyer and the base plate are made of the same material, the impact process is symmetric, and the particle velocity u_b in the base plate is given by:

$$u_b = \frac{v_f}{2} \tag{1}$$

where v_f is the impact velocity of the flyer. From the measurements, the particle velocity u_b in the base plate and the shock wave velocity $D_{s,c}$ in the ceramic specimen can be obtained. For the copper base plate at the impact interface, the following relation holds:

$$P_{H,b} = \rho_{0,b}\left[C_{0,b} + \lambda_b\left(2u_b - u_c\right)\right]\left(2u_b - u_c\right) \tag{2}$$

where u_c is the particle velocity in the ceramic, and $\rho_{0,b}$, $C_{0,b}$, λ_b, and $P_{H,b}$ are the density, sound velocity, Hugoniot parameter, and impact pressure of the base plate, respectively. These material parameters are listed in Table 2.

Table 2. Hugoniot parameters for OFHC and Ta.

Material	Density, $\rho_{0,b}$ (kg/m^3)	Sound locity, $C_{0,b}$ (m/s)	λ_b
OFHC	8935	3933	1.50
Ta	16656	3293	1.31

For the impact interface of the ceramic specimen, the following relation holds:

$$P_{H,c} = \rho_{0,c} D_{s,c} u_c \tag{3}$$

where $P_{H,c}$ is the impact pressure on the ceramic, and $\rho_{0,c}$ is the initial density of the ceramic. From the continuity condition at the interface ($P_{H,b}$=$P_{H,c}$), the particle velocity u_c can be obtained by substituting into Equation (3).

$$u_c = \frac{-b \pm \sqrt{b^2 - 4ac}}{2a} \tag{4}$$

where:

$$\begin{cases} a = \rho_{0,b}\lambda_b \\ b = -\left(\rho_{0,b}C_{0,b} + \rho_{0,c}D_{s,c} + 4\lambda_b u_b \rho_{0,b}\right) \\ c = 2\rho_{0,b}u_b\left(C_{0,b} + 2\lambda_b u_b\right) \end{cases} \tag{5}$$

Substituting the shock wave velocity $D_{s,c}$ and the particle velocity u_c of the ceramic into the above equations yields the impact pressure $P_{H,c}$ generated by the collision. The value $2u_{HEL}$ (the critical free surface velocity of the specimen at the transition from elastic to inelastic response) is used to characterize the confined yield strength of the material.

When the material reaches the HEL state, its density, particle velocity, and other parameters re-enter equilibrium. The density and HEL under the Hugoniot state are given by:

$$\mathrm{HEL} = \rho_{0,\mathrm{c}} C_{\mathrm{H,c}} u_{\mathrm{HEL}} \tag{6}$$

where $C_{\mathrm{H,c}}$ is the sound velocity of the ceramic. The plate impact results are summarized in Table 3.

Table 3. Hugoniot parameters for OFHC and Ta.

NO.	Flyer	v_f (m/s)	u_{HEL} (m/s)	$D_{H,c}$ (m/s)	$D_{s,c}$ (m/s)	u (m/s)	ρ_H (kg/m³)	HEL (GPa)	μ	$P_{H,c}$ (GPa)
1	SiC	580	-	10890	9130	327	3197	-	0.0214	9.34
2	Cu	1010	434	10630	9320	592	3290	15.98	0.0511	17.27
3	Cu	1410	544	10780	9440	839	3370	20.01	0.0767	24.79
4	Cu	1740	-	-	9650	994	3426	-	0.0946	30.02
5	Ta	1970	-	-	9880	1354	3518	-	0.1240	42.28

The HEL of the pressureless-sintered SiC ceramic was 18 GPa. u_{HEL} is illustrated in Figure 3.

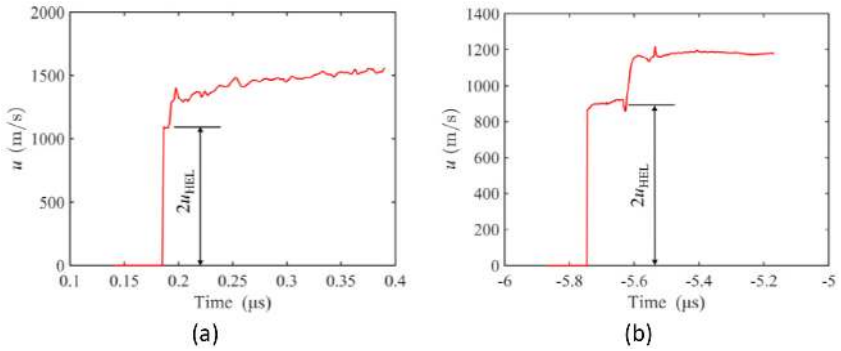


Figure 3 Photograph of the single-stage hydrogen-oxygen gun: (a) vf=1410 m/s and (b) vf=1010 m/s

Other thermodynamic parameters of the material under the HEL state can be obtained from the *D*-*u* relationship. For materials in the moderate-to-high pressure range without shock-induced phase transition, the *D*-*u* relation (the simplest shock adiabat) is linear, as expressed below:

$$D = C_0 + \lambda u \tag{7}$$

The fitting results are presented in Figure 4, giving C_0=8877 m/s, λ=0.713.

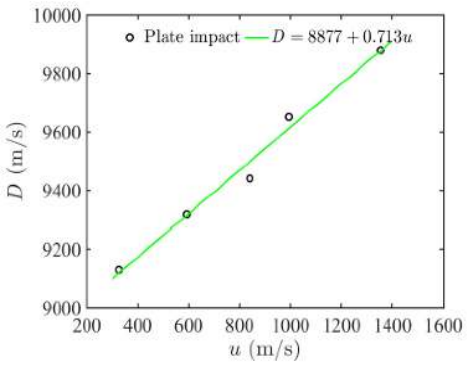


Figure 4 Linear fitting of wave velocity and free surface particle velocity for SiC.

2.3 Dynamic and quasi-static mechanical properties tests

To obtain the strength model parameters of the SiC ceramic in its undamaged state, uniaxial compression experiments were conducted using an Instron universal testing machine and a SHPB. By adjusting the loading speed of the Instron machine, compressive loading under quasi-static conditions was achieved at various strain rates (from 10^{-3} to 10^{-1} s^{-1}). The dynamic compression experiments were performed on the SHPB system, in which both the incident and transmission bars were made of 18Ni spring steel, each with a length of 1500 mm and a diameter of 14.5 mm. The strain rate of the specimens was controlled by varying the launching pressure to adjust the velocity of the striker bar (300 mm in length and 14.5 mm in diameter).

During dynamic compression testing of high-strength materials, if the specimen is in direct contact with the incident bar and the transmission bar, the high strength of the specimen can cause indentations on the bar ends. The formation of these indentations not only damages the testing equipment but also leads to inaccurate experimental results. Therefore, this phenomenon must be avoided during testing. A commonly adopted solution is to place high-strength pads between the specimen and the bars. In dynamic compression tests, the pad material is required not only to possess high strength but also to have suitable damping characteristics, so that stress waves can propagate between the bar and the pad without significant reflection, thereby enhancing the energy absorption capacity of the specimen. However, high-strength, high-hardness pads tend to be relatively brittle. If the pad fractures, it can distort the transmitted stress wave signals and also cause damage to the testing bars. To address this issue, in this study, tungsten carbide (WC) was embedded into 18Ni, the same material as the incident bar, to serve as the pad. An interference fit was employed during embedding to enhance the strength and toughness of the pad. The thickness of the tungsten carbide layer is 2 mm, and the total thickness of the pad is 4 mm. The tungsten carbide contains 88% tungsten, with a yield strength greater than 3 GPa and a hardness of 93 HRA. Blank test verification showed that only the incident signal could be detected in the incident bar, with no reflected signal observed; meanwhile, the transmitted signal captured in the transmission bar was consistent with the incident signal in the incident bar. This fully demonstrates that the wave impedance of the pad matches that of the bar material, satisfying the testing requirements. In addition, pulse shapers were employed in the experiments. Appropriate pulse shapers can reduce inertia effects, achieve dynamic equilibrium conditions, and fulfill constant strain rate requirements. By comparing the stress difference between the front and rear faces of the ceramic specimen using the three-wave method, it was determined whether the stress equilibrium state was achieved. The constant strain-rate condition was assessed by observing whether a plateau existed in the reflected wave. After multiple comparative tests, brass pulse shapers (ϕ4 mm × 2 mm) were ultimately selected. Furthermore, to minimize the constraint effect caused by friction during testing, a thin layer of lubricating grease was uniformly applied to both ends of the specimen.

Similarly, for quasi-static compression tests conducted using an electronic universal material testing machine, in order to protect the machine's indenter and obtain accurate test results, this study employed tungsten carbide pads constrained by high-strength steel. These pads are larger in size and are constrained to move only along the loading direction (i.e., axial direction).

Figure 5 shows the hardened inserts used in mechanical property tests.

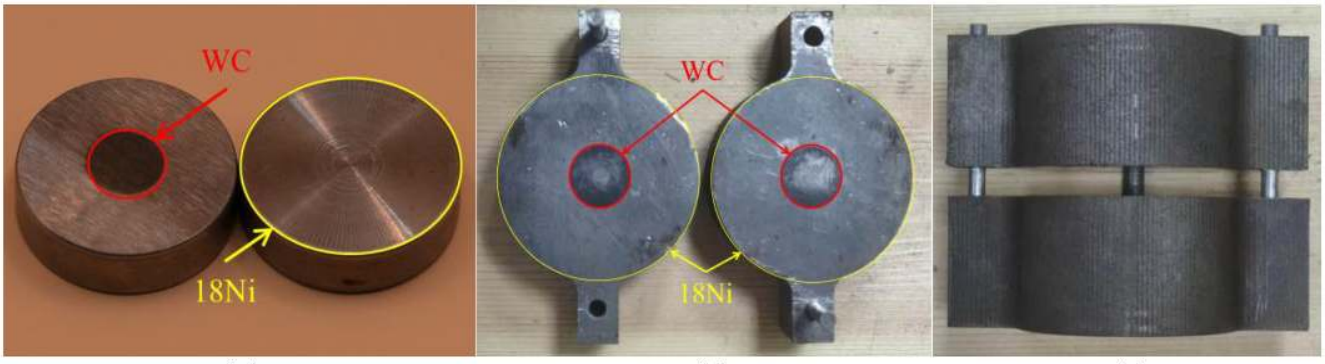


Figure 5 Hardened inserts used in mechanical property tests: (a) WC-hardened insert used in SHPB tests; (b) WC-hardened insert used in quasi-static tests; (c) mounting method of the hardened insert in quasi-static tests.

The resulting true stress-true strain curves are shown in Figure 6.

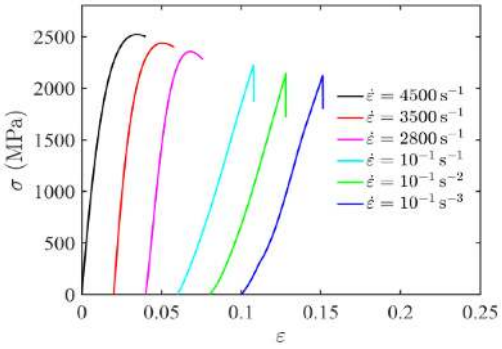


Figure 6 Dynamic stress-strain curves of the ceramic.

3 DESCRIPTION OF THE JH-2 CERAMIC CONSTITUTIVE MODEL AND DETERMINATION OF CONSTANTS

The JH-2 model introduces a damage evolution process as its key enhancement to describe material strength and damage. Strength and pressure are normalized by the HEL stress, which makes most parameters dimensionless and allows for direct comparison across different materials. The model comprises three components: pressure, strength, and failure. The equation of state links volumetric strain to hydrostatic pressure. The strength component describes how the normalized strength varies with normalized pressure and strain rate, both before and after damage occurs. As the damage factor increases, the material strength progressively degrades—meaning strength decreases with increasing plastic strain. The failure component captures the transition from an intact state to complete failure.

3.1 Pressure

The equation of state describes the relationship between volumetric strain and hydrostatic pressure. Under low-velocity impact, where the hydrostatic pressure is relatively small, a simple linear form of the equation of state is sufficient. However, because a reasonably accurate high-pressure equation of state is needed when determining the damage function, a cubic polynomial form is adopted. When the material is undamaged (damage factor D_c=0), the relationship between hydrostatic pressure P and volumetric strain μ in the JH-2 constitutive model can be expressed as:

$$P=K_1\mu+K_2\mu^2+K_3\mu^3 \tag{8}$$

where K_1 is the bulk modulus of the material, and K_2 and K_3 are material constants to be determined.

In the JH-2 model, the volumetric strain μ is defined as:

$$\mu=\frac{\rho_c}{\rho_{0,c}}-1 \tag{9}$$

where ρ_c and $\rho_{0,c}$ are the density of the ceramic under shock compression and its initial density, respectively.

Once damage initiates in the material (D_c>0), radial expansion of the ceramic occurs, and a correction term ΔP must be added after the polynomial.

$$P=K_1\mu+K_2\mu^2+K_3\mu^3+\Delta P \tag{10}$$

From an energy conversion perspective, the reduction in elastic energy is converted into internal potential energy of the material through the pressure increment. The energy conversion equation can be expressed as:

$$(\Delta P_{t+\Delta t}-\Delta P_t)\mu_{t+\Delta t}+(\Delta P_{t+\Delta t}^2-\Delta P_t^2)/(2K_1)=\beta\Delta U \tag{11}$$

where β is the conversion coefficient that transforms elastic energy into potential energy, and U is the internal energy.

The first term $(\Delta P_{t+\Delta t}-\Delta P_t)/\mu_{t+\Delta t}$ in the equation represents the approximate potential energy when μ>0, and the second term correspondingly represents the hydrostatic potential energy when μ<0. As in the JH-1 model, the JH-2 model also takes ΔP=0 when β=0, where β denotes the fraction of lost elastic energy converted into hydrostatic potential energy ($0\le\beta\le1$).

Solving the above equation yields:

$$\Delta P_{t+\Delta t} = -K_1\mu_{t+\Delta t} + \sqrt{(K_1\mu_{t+\Delta t} + \Delta P_t)^2 + 2\beta K_1 \Delta U} \tag{12}$$

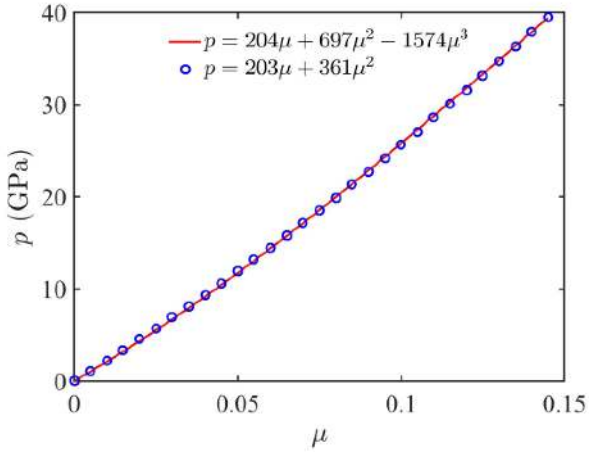


Figure 7 Relationship between volumetric strain and shock pressure in the ceramic.

The *P*-μ curve obtained from plate impact tests reflects the stress state under one-dimensional strain, which contains both hydrostatic and deviatoric stress components. Therefore, it is difficult to directly decouple the relationship between hydrostatic pressure and volumetric strain. In contrast, diamond anvil cell experiments can directly capture the volumetric response under quasi-static pressure, as demonstrated by Bassett et al. (1993). Determining the pressure-volumetric-strain relationship for ceramic materials has long been a challenge. To address this, a fitting approach was adopted based on the literature data (Lahiri et al. 2019). The fitting results are shown in Figure 7, yielding parameters of K_2=697GPa, K_3=−1574GPa.

3.2 Strength

In the JH-2 model, the strength and pressure are normalized by the hydrostatic pressure P_{HEL} and the equivalent stress σ_{HEL} at the HEL, respectively. Therefore, accurate determination of these two parameters is required. The HEL stress state can be decomposed into a hydrostatic pressure component and a deviatoric stress component, as expressed below:

$$\mathrm{HEL} = P_{\mathrm{HEL}} + \frac{2\sigma_{\mathrm{HEL}}}{3} \tag{13}$$

P_{HEL} can be obtained using Equation (8), and σ_{HEL} can be obtained from the relationship between the deviatoric stress tensor and volumetric strain through Hooke's law:

$$\sigma_{\mathrm{HEL}} = \frac{2G\mu_{\mathrm{HEL}}}{1+\mu_{\mathrm{HEL}}} \tag{14}$$

where *G* is the shear modulus. Substituting Equations (14) and (8) into Equation (13) yields:

$$\mathrm{HEL} = K_1\mu_{\mathrm{HEL}} + K_2\mu_{\mathrm{HEL}}^2 + K_3\mu_{\mathrm{HEL}}^3 + \frac{4G\mu_{\mathrm{HEL}}}{3(1+\mu_{\mathrm{HEL}})} \tag{15}$$

From the plate impact tests, the HEL of the material was determined to be 18 GPa. According to Equation (15), μ_{HEL}=0.03979 was obtained, and substituting it into Equations (14) and (8) yields P_{HEL}=9.12 GPa, σ_{HEL}=13.32 GPa.

The JH-2 strength model expresses the equivalent stress of the material as a power law function of the hydrostatic pressure, and also incorporates the effects of strain rate and the damage factor D_c. The normalized strength model is defined as follows:

$$\sigma^* = \sigma_{i,c}^* - D_c(\sigma_{i,c}^* - \sigma_{f,c}^*) \tag{16}$$

where $\sigma_{i,c}^*$ denotes the normalized intact equivalent stress, $\sigma_{f,c}^*$ denotes the normalized fractured equivalent stress, and $0 \le D_c \le 1$ represents the damage factor of the SiC ceramic. $\sigma^* = \sigma/\sigma_{HEL}$ is the normalized equivalent stress, and the equivalent stress σ is calculated by the Von Mises criterion (Wang et al. 2018):

$$\sigma = \sqrt{1/2\left[(\sigma_x - \sigma_y)^2 + (\sigma_x - \sigma_z)^2 + (\sigma_y - \sigma_z)^2 + 6(\tau_{xy}^2 + \tau_{xz}^2 + \tau_{yz}^2)\right]} \tag{17}$$

where σ_x, σ_y, and σ_z are the three normal stresses, and τ_{xy}, τ_{xz}, and τ_{yz} are the three shear stresses.

Under undamaged conditions, the normalized equivalent stress is formulated as:

$$\sigma_{i,c}^* = A_c\left(P_c^* + T_c^*\right)^{N_c}\left(1 + C_c \ln \dot{\varepsilon}^*\right) \tag{18}$$

The normalized fracture stress is defined as:

$$\sigma_{f,c}^* = B_c\left(P_c^*\right)^{M_c}\left(1 + C_c \ln \dot{\varepsilon}^*\right) \ , \ \sigma_{f,c}^* \le \sigma_{fmax}^* \tag{19}$$

where A_c, B_c, C_c, M_c, and N_c are material constants. Stresses are normalized by σ_{HEL}, while pressure is normalized by P_{HEL}. $T_c^* = T_c/P_{HEL}$ is the normalized tensile strength, where T_c is the hydrostatic tensile limit. The normalized pressure is $P_c^* = P_c/P_{HEL}$, with P_c being the equivalent hydrostatic pressure, which is one third of the compressive strength under uniaxial compression. The dimensionless strain rate is $\dot{\varepsilon}^* = \dot{\varepsilon}/\dot{\varepsilon}_0$, where $\dot{\varepsilon}$ is the actual strain rate and $\dot{\varepsilon}_0$ is the reference strain rate. In this paper, the reference strain rate $\dot{\varepsilon}_0$ is taken as 1 s^{-1}. In plate impact tests, the strain rate $\dot{\varepsilon}$ under the HEL state is typically taken as 10^5 s^{-1}(Grady 1998). The results of the uniaxial compression tests are summarized in Table 4.

Table 4. Quasi-static and dynamic compression test results.

NO.	$\dot{\varepsilon}$ (s^{-1})	σ_c (MPa)	P_c (MPa)	σ_c^*	P_c^*
Instron 1#	0.001	2122	707	0.1593	0.0776
Instron 2#	0.01	2142	714	0.1608	0.0783
Instron 3#	0.1	2226	742	0.1671	0.0814
SHPB 1#	2800	2358	786	0.1770	0.0862
SHPB 2#	3500	2438	813	0.1830	0.0891
SHPB 3#	4500	2522	841	0.1893	0.0922
HEL	10^5	13320	9120	1	1

The strain-rate sensitivity constant C_c was calibrated using the uniaxial compression test data. The linear fitting result is shown in Figure 8, yielding C_c =0.01.

The pressure and strength data at the HEL state, together with an additional set of data, are typically used to determine the parameters A_c and N_c. In the present work, a fitting method is adopted. Taking the logarithm of both sides of Equation (18) and rearranging yields:

$$\ln \sigma_{i,c}^* - \ln\left(1 + C_c \ln \dot{\varepsilon}^*\right) = \ln A_c + N_c \ln\left(P_c^* + T_c^*\right) \tag{20}$$

with T_c^* =0.0285, substituting the data in Table 4 into Equation (20), the linear fitting result is shown in Figure 9, yielding A_c=0.874, N_c=0.750.

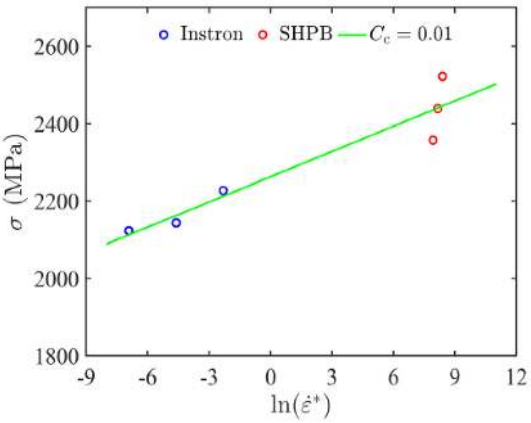


Figure 8 Strain rate sensitivity and constant determination for SiC.

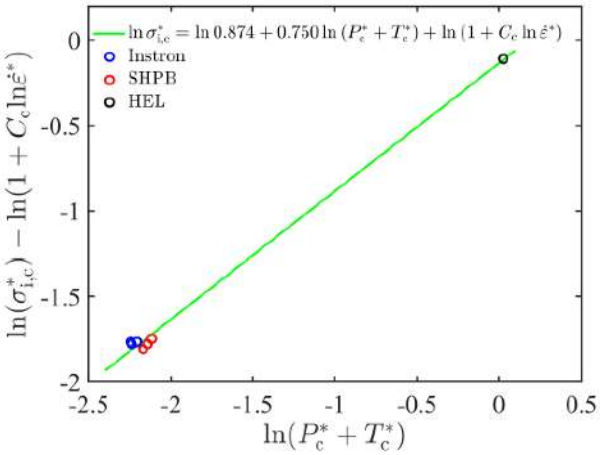


Figure 9 Fitting results of JH-2 strength model parameters.

It is difficult to determine the fractured material strength parameters B_c and M_c. Through pre-calculation, the parameters that best fit the experimental results were obtained as B_c =0.35 and M_c =0.5. Figure 10 presents the JH-2 strength model and test data derived above. The intact strength of the JH-2 model at strain rates ($\dot{\varepsilon}$=10^{-3} and 10^5 s^{-1}) corresponds to the undamaged material (D_c=0). For the fully damaged material (D_c=1.0), the fractured material strength is shown at strain rate ($\dot{\varepsilon}_0$ =1 s^{-1}).

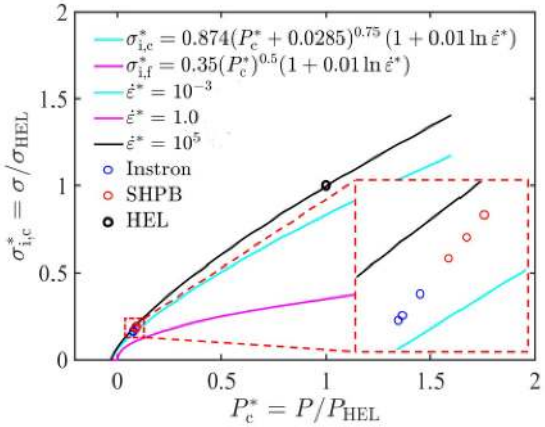


Figure 10 Test data and model for the strength of SiC.

3.3 Damage

The damage in the JH-2 model is described by a damage variable, which represents the damage state within a specific material volume (i.e., an element). During material deformation, the damage variable gradually evolves, leading to a reduction in material strength. At the same time, both the material strength and the degree of damage depend on the pressure at the given location. Similar to the Johnson-Cook damage model (Johnson 1985), the damage factor D_c in the JH 2 model can be concisely expressed as:

$$D_c = \sum \frac{\Delta \varepsilon_P}{\varepsilon_p^f} \tag{21}$$

where $\Delta\varepsilon_p$ is the accumulated effective plastic strain within a single cycle, and ε_p^f is the equivalent plastic strain at fracture under a given pressure, expressed as:

$$\varepsilon_p^f = D_{1,c}(P_c^* + T_c^*)^{D_{2,c}} \tag{22}$$

Therefore, the damage parameters $D_{1,c}$ and $D_{2,c}$ are introduced in the JH-2 damage model. Since ceramics tend to fracture at relatively small strains, it is difficult to obtain the values of $D_{1,c}$ and $D_{2,c}$ experimentally. Instead, these damage functions are indirectly back-calculated using various methods (Holmquist et al. 1995, 2001).

The equivalent plastic strain is calculated as follows:

$$\varepsilon_p^f = \sqrt{2/9\left[\left(\varepsilon_x^f - \varepsilon_y^f\right)^2 + \left(\varepsilon_x^f - \varepsilon_z^f\right)^2 + \left(\varepsilon_y^f - \varepsilon_z^f\right)^2 + 3/2\left(\gamma_{xy}^{f\,2} + \gamma_{xz}^{f\,2} + \gamma_{yz}^{f\,2}\right)\right]} \tag{23}$$

where ε_x^f, ε_y^f and ε_z^f are the three normal strains, and γ_{xy}^f , γ_{xz}^f and γ_{yz}^f are the three shear strains. Under uniaxial compression, Equation (23) can be simplified as:

$$\varepsilon_p^f = 2\varepsilon_z^f / 3 \tag{24}$$

The plastic strain (ε_z^f) required for complete material failure is defined as (Holmquist et al. 2001):

$$\varepsilon_z^f = \varepsilon_z^{pla} / D_c \tag{25}$$

where ε_z^{pla} is the plastic strain, which can be obtained from the total strain ε_z^{total} and the elastic strain ε_z^{ela}, i.e., $\varepsilon_z^{pla}=\varepsilon_z^{total}-\varepsilon_z^{ela}$. The damage factor D_c can be obtained from Equation (16), i.e.,

$$D_c = \left(\sigma_{i,c}^* - \sigma_c^*\right)\left(\sigma_i - \sigma_{f,c}^*\right) \tag{26}$$

$\sigma^*_{i,c}$ and $\sigma^*_{f,c}$ can be obtained from Equations (18) and (19). The normalized equivalent stress is calculated as follows:

$$\sigma_c^* = \frac{3(\sigma_z - P_c)}{2\sigma_{HEL}} \tag{27}$$

The total uniaxial strain ε_z^{total} (compression taken as positive) is determined by the following equation:

$$\varepsilon_z^{total} = \mu / (1+\mu) \tag{28}$$

For the elastic strain ε_z^{ela}, assuming the ceramic remains elastic before reaching the HEL state in the tests, the value can be obtained by substituting μ_{HEL} into Equation (28) .

Finally, the fracture equivalent plastic strain obtained from the plate impact tests is shown in Table 5, where σ_z denotes the ceramic impact pressure $P_{H,c}$.

Table 5. Fracture strain determination from plate impact results.

σ_z	μ	P_c (GPa)	σ_c^*	$\sigma_{i,c}^*$	$\sigma_{f,c}^*$	u (m/s)	ε_z^{total}	ε_z^{pla}	ε_z^f	ε_p^f
9.34	0.0214	4.67	0.526	0.614	0.279	262	0.0210	-	-	-
17.27	0.0511	12.02	0.592	1.218	0.448	814	0.0486	0.0103	0.0127	0.0085
24.79	0.0767	18.98	0.654	1.706	0.563	921	0.0712	0.0329	0.0358	0.0239
30.02	0.0946	24.13	0.664	2.038	0.635	980	0.0864	0.0481	0.0491	0.0328
41.88	0.1240	32.90	1.0115	2.566	0.741	852	0.1103	0.0720	0.0845	0.0564

Taking the logarithm of Equation (22) yields:

$$\ln \varepsilon_p^f = \ln D_{1,c} + D_{2,c} \ln (P_c^* + T_c^*) \tag{29}$$

Fitting the experimental data gives the parameters $D_{1,c}$ and $D_{2,c}$. The fitting results are shown in Figure 11, yielding $D_{1,c}$ =0.00516, $D_{2,c}$ =1.8895.

By integrating the mechanical response data obtained from the quasi-static compression, dynamic compression, and plate impact tests, and following the calibration procedure for the JH-2 model parameters, the complete set of JH-2 constitutive parameters for the sintered SiC ceramic was determined. The specific values are listed in Table 6.

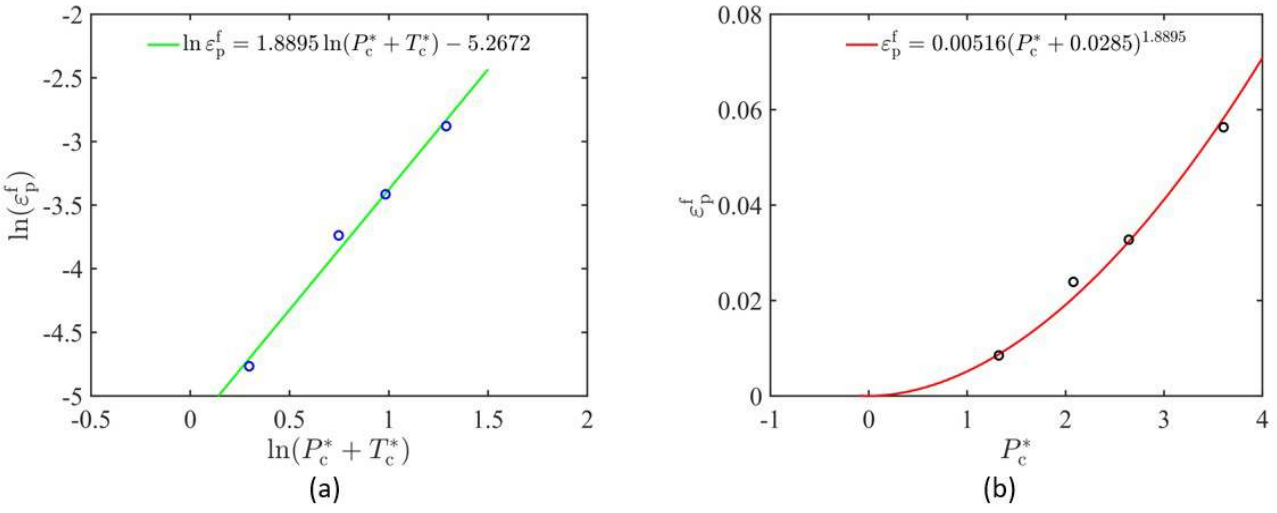


Figure 11 Model for the damage behavior of SiC: (a) Fitting of the JH-2 damage model parameters $D_{1,c}$ and $D_{2,c}$; (b) Normalized hydrostatic pressure-equivalent racture strain relationship for the material.

Table 6. JH-2 constitutive model parameters for SiC

$\rho_{0,c}$(kg/m^3)	G(GPa)	A_c	N_c	C_c	B_c	M_c	T_c(GPa)	P_{HEL}(GPa)
3130	172	0.874	0.750	0.01	0.35	0.50	0.26	9.12
$D_{1,c}$	$D_{2,c}$	K_1(GPa)	K_2(GPa)	K_3(GPa)	HEL (GPa)	β	$\dot{\varepsilon}_0$ (s^{-1})	
0.00516	1.8895	204	697	-1574	18	1.0	1.0	

4 CONSTITUTIVE MODEL VALIDATION AND THE PENETRATION RESISTANCE OF SIC CERAMIC AGAINST TUNGSTEN ALLOY

The JH-2 constitutive parameters of the SiC ceramic were calibrated through quasi-static compression, dynamic compression, and plate impact tests. To verify the accuracy and applicability of the model under impact loading conditions, the present section conducts numerical simulations and ballistic tests based on these parameters. First, a numerical simulation model is established using the explicit finite element software ABAQUS, and the reliability of the JH-2 model parameters is validated by comparison with the experimentally measured depths of penetration. The penetration resistance of the SiC ceramic against fragments of three different shapes at various impact velocities is systematically analyzed, and the effects of fragment velocity and fragment shape on the protective performance of the ceramic are discussed. The results of this study can provide theoretical support and data for the application of SiC ceramics in lightweight composite armor.

The penetration resistance can be investigated through ballistic penetration tests. Owing to the inherent brittleness of ceramic materials, they are often used in combination with a metallic backing plate in practical protective structures. Therefore, the residual penetration depth test is commonly employed to evaluate their penetration resistance. In this method, the protective effect of the ceramic layer is characterized by measuring the residual penetration depth of the projectile into the metallic backing plate after penetrating the ceramic/metal composite target. The ballistic protection coefficient η of the ceramic against penetration is defined as:

$$\eta = \frac{\rho_{\mathrm{b}}\left(P_{\mathrm{b}} - P_{\mathrm{res}}\right)}{\rho_{\mathrm{c}} h_{\mathrm{c}}} \tag{30}$$

where ρ_{c} and h_{c} are the density and thickness of the ceramic, respectively; P_{res} is the residual penetration depth of the projectile into the metallic backing plate after penetrating the ceramic/metal composite target; P_{b} is the penetration depth of the projectile into the metallic backing plate (without the ceramic layer); and ρ_{b} is the density of the metallic backing plate.

The metallic backing plate is typically made of rolled homogeneous armor (RHA) or aluminum alloy, with the former being suitable for long rod projectiles and the latter for projectiles with a small length-to-diameter ratio. The present study adopts 6061-T6 aluminum alloy as the material for the metallic backing plate. The calculation of the ballistic protection coefficient η depends on two key quantities: Pres and Pb. Therefore, two cases are set up in both numerical simulations and ballistic tests: Case 1 involves fragment penetration into the SiC/6061-T6 composite target to measure Pres, and Case 2 involves fragment penetration into the 6061-T6 aluminum alloy target to measure Pb.

4.1 Computations

To validate the reliability of the JH-2 model parameters calibrated and to further investigate the penetration resistance of SiC ceramic against fragments, numerical simulation models were established for tungsten alloy fragment penetration into 6061-T6 aluminum alloy and SiC/6061-T6 composite targets. The JH-2 constitutive model parameters of the SiC ceramic (except for the fractured strength parameters) were all calibrated based on experimental data, and the specific values are summarized in Table 6. Ballistic impact numerical simulations were conducted using the JH-2 model with the calibrated parameters, and the computed results were compared with penetration test data to verify the reliability of the numerical simulations and the accuracy of the material parameters.

4.1.1 Finite element model

The nonlinear dynamic finite element program ABAQUS/Explicit was used to analyze the penetration process of 93W tungsten alloy (93W-4.9Ni-2.1Fe) fragments into 6061-T6 aluminum alloy and SiC/6061-T6 composite targets. The Lagrangian formulation was employed to describe the dynamic deformation and failure behavior of the fragment, the 6061-T6 aluminum alloy, and the SiC ceramic. Although normal penetration was considered, possible trajectory deflection during penetration necessitated the use of a full-scale model. The dimensions of the 6061-T6 aluminum alloy target were 100 mm × 100 mm × 100 mm, and those of the SiC ceramic were 50 mm × 50 mm × 6 mm. A counterbore pocket of 50.2 mm × 50.2 mm × 6.2 mm was milled in the aluminum alloy to accommodate the ceramic. The fragments included a sphere of 10 mm diameter, a cylinder of 8.74 mm diameter and 8.74 mm height, and a cube with a side length of 8.06 mm. The spherical fragment had no issue of impact attitude, while the cubic and cylindrical fragments were set to penetrate axially. The finite element models of the fragments and the ceramic composite target were all meshed with 8-node hexahedral fully integrated elements (C3D8I). C3D8I elements were selected to avoid shear locking and hourglass instabilities while maintaining reasonable computational efficiency. Mesh convergence analysis shows that as the

aluminium alloy target mesh size is progressively refined from 1.5 mm to 0.5 mm, the penetration depth converges at the 0.75 mm mesh size, with negligible further change when refining to 0.5 mm. The fragment itself was also meshed with a uniform element size of 0.75 mm. To improve computational accuracy, local mesh refinement was performed in the central region of the target, with a refined mesh size of 0.75 mm × 0.75 mm × 0.75 mm over an area of 25 mm × 25 mm—sufficiently larger than the projectile cross-sectional area to fully cover the high-strain zone. The regions away from the centre were meshed with coarser elements, with the element size gradually increasing toward the edges of the target. The ceramic layer was tied to the aluminium alloy back plate using a cohesive contact definition (or Tie constraint) to model interfacial bonding, while the lateral faces of the target were left as free boundaries. The bottom surface of the aluminium alloy back plate was fully fixed in all degrees of freedom to simulate a rigid support condition. The finite element model of the fragment and the ceramic composite target is shown in Figure 12.

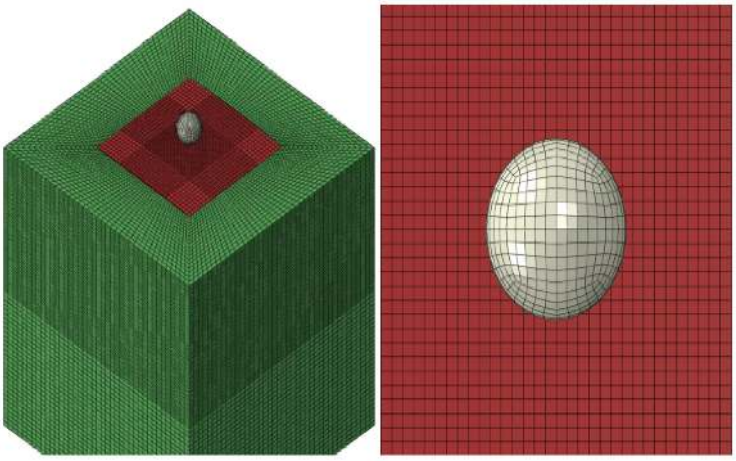


Figure 12 Finite element model.

4.1.2 Material models

During fragments penetration into the target plate, both the 93W tungsten alloy (93W-4.9Ni-2.1Fe) and the 6061-T6 aluminum alloy underwent extreme conditions involving large deformation, high strain rates, high pressure, and high temperature. Therefore, the Johnson-Cook (J-C) constitutive model was employed to describe their behavior. The J-C model was proposed by Johnson and Cook in 1983 (Johnson 1985) as an empirical constitutive model for describing the mechanical behavior of metallic materials under high strain rates, large deformation, and elevated temperatures. Its feature lies in decoupling the three effects—strain hardening (strain term), strain rate strengthening (strain-rate term), and thermal softening (temperature term)—through a multiplicative form, intuitively representing the material behavior in which strength increases with increasing strain and strain rate but decreases with increasing temperature. The J–C constitutive model adopted herein offers clear physical interpretations for its parameters and is straightforward to calibrate; moreover, it is natively implemented in ABAQUS. Within this framework, damage initiation is governed by the J–C damage initiation criterion (keyword *Damage Initiation, criterion=JOHNSON COOK). In the damage evolution stage, a displacement-based failure criterion (keyword *Damage Evolution, type=DISPLACEMENT) is adopted, whereby an element is considered to have completely failed and is deleted from the computation when the cumulative displacement at its integration point reaches a predefined critical value. To account for volumetric response under high pressure, the classical Mie-Grüneisen equation of state (EOS) was employed for the tungsten alloy and the 6061-T6 aluminium alloy. The J-C model parameters, damage evolution parameters, and EOS coefficients for these two materials are summarised in Table 7.

Table 7. J-C strength model constants and Mie-Grüneisen EOS constants for materials used in the DOP ballistic computations.

Material	ρ(kg/m^3)	A_m (MPa)	B_c (MPa)	C_m	N_m	M_m	T_M(K)	c_0(m/s)	s_1
93W (Lundberg et al. 2005)	17700	631	1258	0.092	0.014	0.94	1723	3940	1.54
6061-T6 (Robbins et al. 2004)	2704	324	114	0.42	0.002	1.34	878	5240	1.40

4.2 Penetration

To validate the JH-2 constitutive model of the SiC ceramic, ballistic penetration tests corresponding to the numerical simulation conditions were conducted, namely the penetration of 93W fragments into 6061-T6 aluminum alloy and SiC/6061-T6 composite targets.

4.2.1 Test setup

The fragments used in the tests were of regular shapes and made of 93W. Three types of fragments were employed: a sphere with a diameter of 10 mm (denoted as S), a cylinder with a diameter of 8.74 mm and a height of 8.74 mm (denoted as B), and a cube with a side length of 8.06 mm (denoted as C). During the tests, the impact attitudes of the cylindrical and cubic fragments were controlled to be consistent with those in the numerical simulations. Sabots made of aluminum alloy and nylon were used primarily to improve the gas-sealing performance of the chamber and to ensure proper positioning of the fragments. The aluminum alloy used in the tests was standard 6061-T6 with target dimensions of 100 mm × 100 mm × 100 mm (denoted as Al). The SiC ceramic specimens measured 50 mm × 50 mm × 6 mm. A square cavity of 50.2 mm × 50.2 mm × 6.1 mm was milled into the 6061-T6 aluminum alloy, and the ceramic was embedded to form the SiC/6061-T6 composite target (denoted as SiC/Al). The fragments and the ceramic composite target are shown in Figure 13:

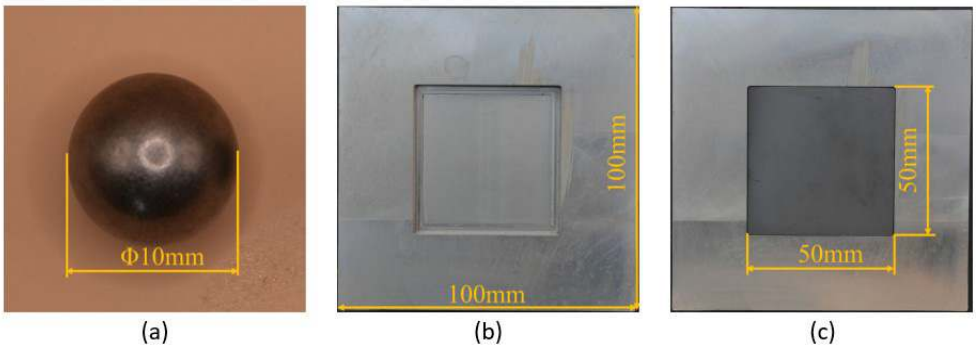


Figure 13 Fragment and target in penetration experiment: (a) Tungsten alloy spherical fragment with a diameter of 10 mm; (b)6061-T6 aluminum alloy backing plate; (c) SiC/Al composite target.

4.2.2 Test method

A forward ballistic test method was adopted, in which fragments were launched to penetrate a stationary target. A schematic diagram of the test layout and a photograph of the setup are shown in Figure 14. During the tests, a 14.5 mm ballistic gun was used to launch the fragments, and the fragment velocity was controlled by varying the mass of the propellant charge. The target plates were placed as shown in Figure 14. High-speed camera was employed to observe the flight process and impact attitude of the fragments, as well as to measure their velocities. In addition, a sabot collector was placed in front of the target to intercept the sabots that separated from the fragments after leaving the gun muzzle.

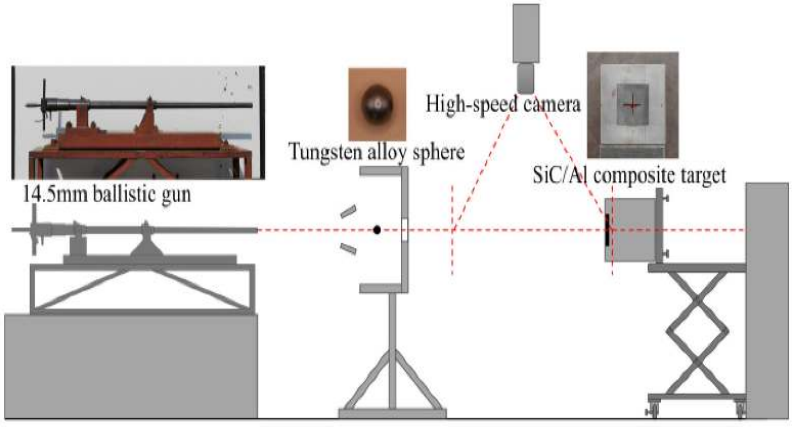


Figure 14 Experimental layout and photograph in penetration experiments.

4.3 Results and discussion

Based on the data of fragment initial velocity and penetration depth obtained from the ballistic penetration tests of tungsten alloy fragments into SiC/Al composite targets, the initial fragment velocities in the numerical simulations were set to be consistent with the test conditions. The reliability of the numerical simulation method and the material model parameters was verified by comparing the numerical results with the experimental data. The validated numerical model was used to systematically analyze the effects of fragment shape and impact velocity on the penetration resistance of the SiC ceramic, as well as the variation pattern of the ceramic protection efficiency

4.3.1 Penetration test results

To accurately obtain the penetration depth and the deformation of the fragments after penetration, the targets were sectioned for measurement and photography. The impact velocity V_0 of the fragment was measured using high-speed camera. After penetrating the SiC/Al composite target, the fragments were partially embedded in the backing plate. The test results are shown in Figure 15. For the composite target, all fragments showed significant deformation and erosion, with the spherical fragment deforming the most, while the cubic and cylindrical fragments deformed less. In contrast, for the monolithic 6061-T6 aluminum target, the opposite trend was observed: the spherical fragment deformed the least (Figure 15(d)), whereas the cylindrical fragment exhibited pronounced upsetting and a “mushroom head” (Figure 15(f)).

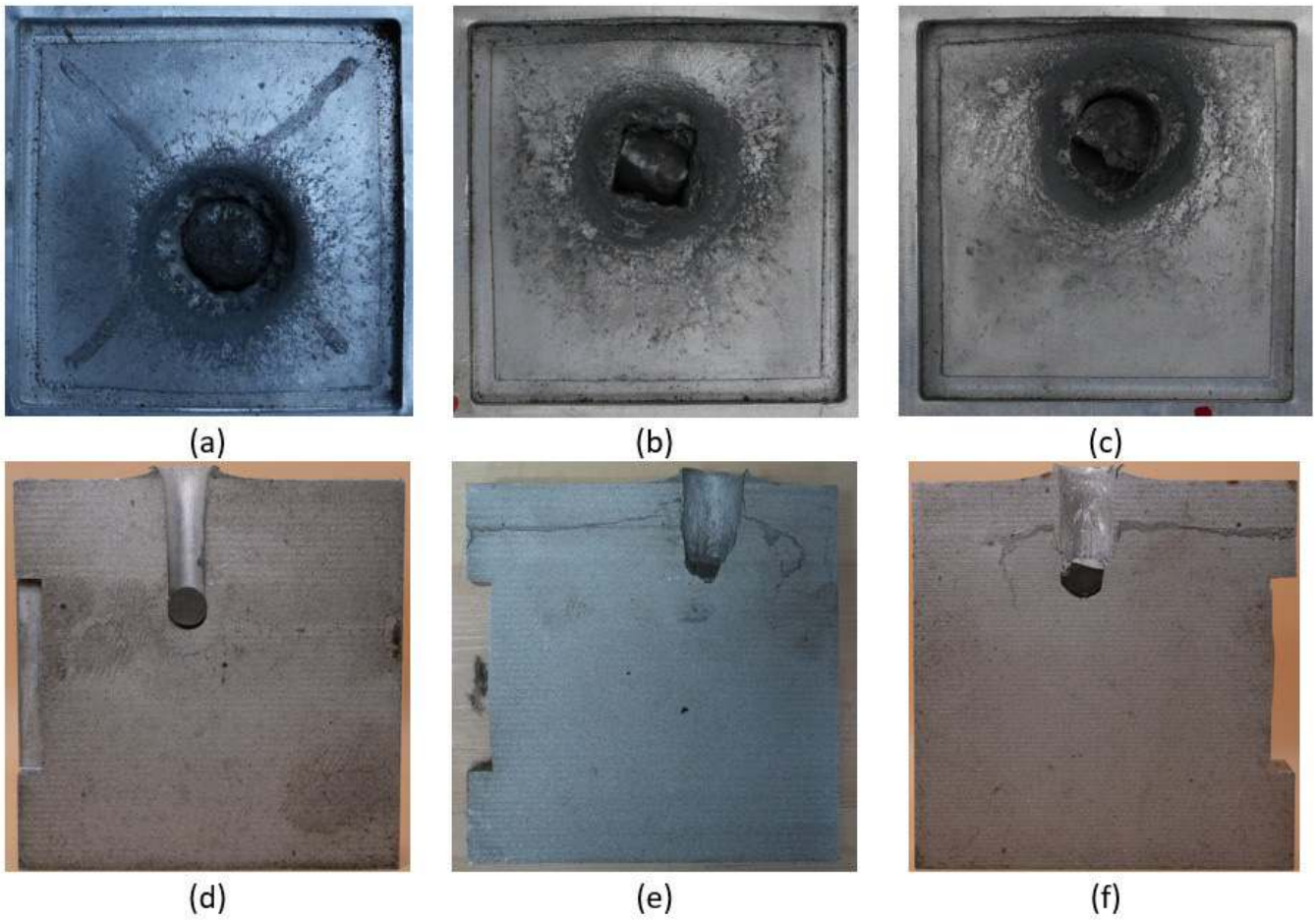


Figure 15 Fragment morphologies after penetrating different targets: (a) S-SiC/Al, V_0=1315; (b) B-SiC/Al, V_0=1183; (c) C-SiC/Al, V_0=1153; (d) S-Al, V_0=1086; (e) B-Al, V_0=1186; (f) C-Al, V_0=1187.

4.3.2 Comparison between numerical simulation and test results

A total of 10 valid sets of data were obtained from the tests. Numerical simulations were first carried out under the same test conditions. The comparison between simulation and test results is shown in Table 8, where P_t and P_s represent the penetration depth measured in tests and obtained from simulations, respectively, and V_0 is the fragment velocity.

As seen in Table 8, the simulated penetration depths of the tungsten alloy fragments into the 6061-T6 aluminum alloy and the SiC/Al composite target under different impact velocities are in good agreement with the test results, with a maximum error of 8.42%.

Figure 16 compares the penetration depth and channel morphology of the spherical fragment penetrating the 6061-T6 aluminum alloy and the SiC/Al composite target. It can be seen that the smoothness of the penetration channel in the numerical simulation differs considerably from that in the test for the 6061-T6 aluminum alloy, which may be attributed to the element deletion treatment in the simulation. Element deletion also affects the secondary penetration of aluminum alloy by ceramic fragments, which is the main reason for the large difference in the channel morphology observed in the aluminum alloy between the simulation and the test when the fragment penetrates the SiC/Al composite target.

Table 8. Comparison between test and numerical simulation results

No.	Target	V_0 (m/s)	P_t (mm)	P_s (mm)	error (%)
S-1#	6061-T6	944	32.0	33.1	3.44
S-2#	6061-T6	1086	39.0	39.7	1.79
S-3#	6061-T6	1106	39.2	40.5	3.32
C-1#	6061-T6	1187	30.3	31.3	3.30
B-1#	6061-T6	1186	27.3	29.6	8.42
S-4#	SiC/Al	929	15.4	16.4	6.49
S-5#	SiC/Al	1112	18.7	20.0	6.95
S-6#	SiC/Al	1315	24.8	25.3	2.02
C-2#	SiC/Al	1153	23.6	24.7	4.66
B-2#	SiC/Al	1183	23.5	25.0	6.38

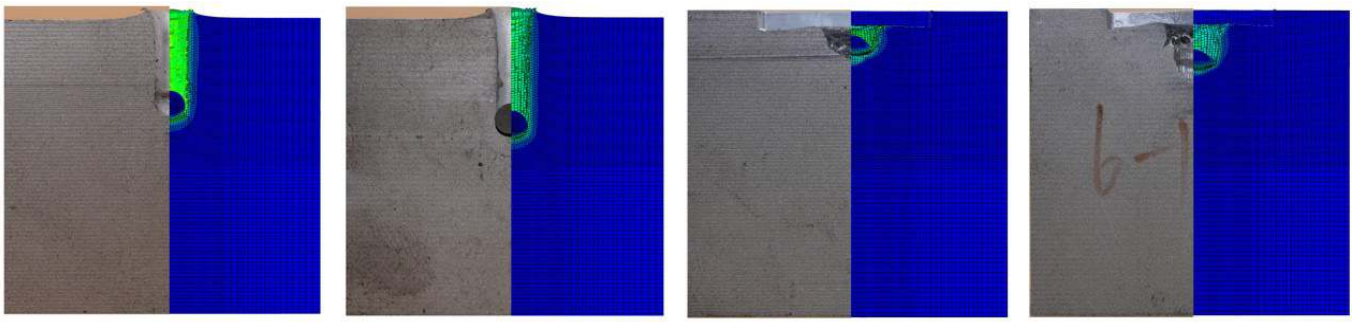


Figure 16 Comparison of penetration results between tests and numerical simulations: (a) S-1#; (b) S-3#;(c) S-4#; (d) S-5#.

In addition, high-speed photography captured the impact orientation of the fragments during penetration, which is known to have a measurable effect on the penetration performance of cylindrical and cubic fragments. The impact attitudes of the fragments are presented in the Figure 17.

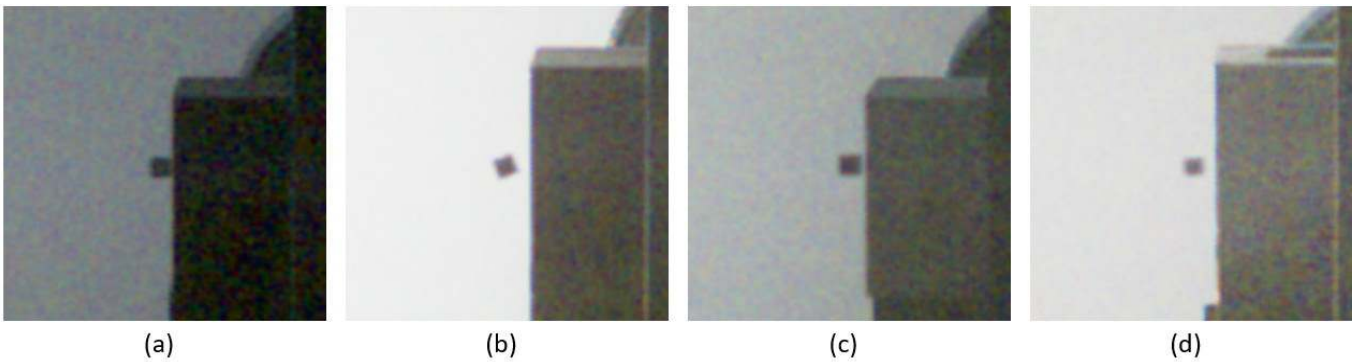


Figure 17 Impact attitude of the fragment recorded by high-speed photography: (a) C-1#; (b) B-1#; (c) C-2#; (d) B-2#.

As can be seen from Figure 17, the impact attitudes of the fragments in Figures 17(a), (c), and (d) can be preliminarily judged as close to axial normal penetration, while that in Figure. 17(b) exhibits a significant deviation. Combined with the observations in Figure 15, it can be confirmed that, except for the fragment in test No. B-1#, all other fragments can be considered to be in a state of near-axial normal penetration. Figure 18 compares the deformation of the spherical fragment after penetrating the SiC/Al composite target between the test and the simulation. It can be seen that the fragment deformation obtained from the simulation is in good agreement with the test result.

Overall, the finite element model and material parameters adopted in this study are reasonable and can adequately simulate the penetration process of fragments into 6061-T6 aluminum alloy targets and SiC/Al composite targets. Therefore, they can be used for further numerical studies on the fragment penetration resistance of SiC ceramics.

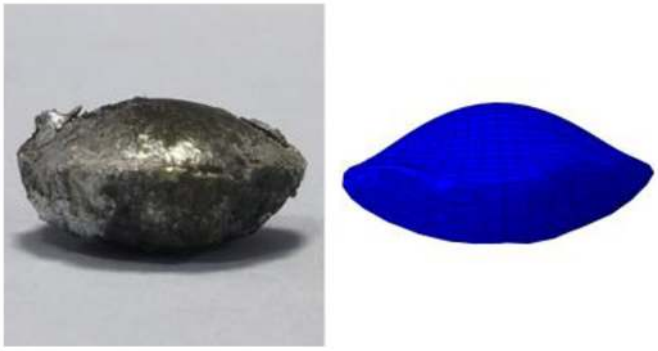


Figure 18 Comparison of fragment deformation between test and numerical simulation (S-6#)

4.3.3 Penetration resistance of SiC ceramic against tungsten alloy fragments

Based on the numerical simulation method described above, the effects of fragment shape and initial velocity on the penetration process into SiC/Al composite targets were investigated. The aim was to reveal the penetration resistance of the ceramic against three types of fragments at different impact velocities, and to provide data support for the optimal design of ceramic composite targets. The fragment specifications were the same as those described previously, and the initial velocities were set to 800, 1000, 1200, and 1400 m/s, respectively. Table 9 summarizes the penetration depths of the three fragment shapes (spherical, cylindrical, and cubic) into the 6061-T6 aluminum alloy and the SiC/Al composite targets at four impact velocities of 800, 1000, 1200, and 1400 m/s. In the table, Pb denotes the penetration depth into the monolithic 6061-T6 aluminum alloy, Pres is the residual penetration depth into the aluminum backing plate of the composite target, and η is the calculated protection coefficient of the ceramic.

Table 9 summarizes the penetration depths of the three fragment shapes (spherical, cylindrical, and cubic) into the 6061-T6 aluminum alloy and the SiC/Al composite targets at four impact velocities of 800, 1000, 1200, and 1400 m/s. In the table, Pb denotes the penetration depth into the monolithic 6061-T6 aluminum alloy, Pres is the residual penetration depth into the aluminum backing plate of the composite target, and η is the calculated protection coefficient of the ceramic.

Table 9. Simulation results of fragments impact on different targets.

Fragment	V_0 (m/s)	Target	P_b(mm)	Target	P_{res}(mm)	η
S	800	6061-T6	25.8	SiC/Al	7.5	2.63
S	1000	6061-T6	37.5	SiC/Al	11.7	3.71
S	1200	6061-T6	46.6	SiC/Al	15.4	4.49
S	1400	6061-T6	50.0	SiC/Al	20.9	4.19
B	800	6061-T6	18.4	SiC/Al	7.8	1.53
B	1000	6061-T6	24.2	SiC/Al	11.9	1.77
B	1200	6061-T6	29.9	SiC/Al	17.6	1.77
B	1400	6061-T6	34.7	SiC/Al	23.1	1.67
C	800	6061-T6	19.9	SiC/Al	7.9	1.73
C	1000	6061-T6	26.0	SiC/Al	13.2	1.84
C	1200	6061-T6	30.7	SiC/Al	19.2	1.66
C	1400	6061-T6	35.9	SiC/Al	25.3	1.53

Based on the penetration depths P_b and residual penetration depths P_{res} listed in Table 9, the curves of these depths as functions of fragment velocity are plotted in Figure 19(a). The protection coefficients η of the ceramic against the three types of fragments at different velocities are shown in Figure 19(b).

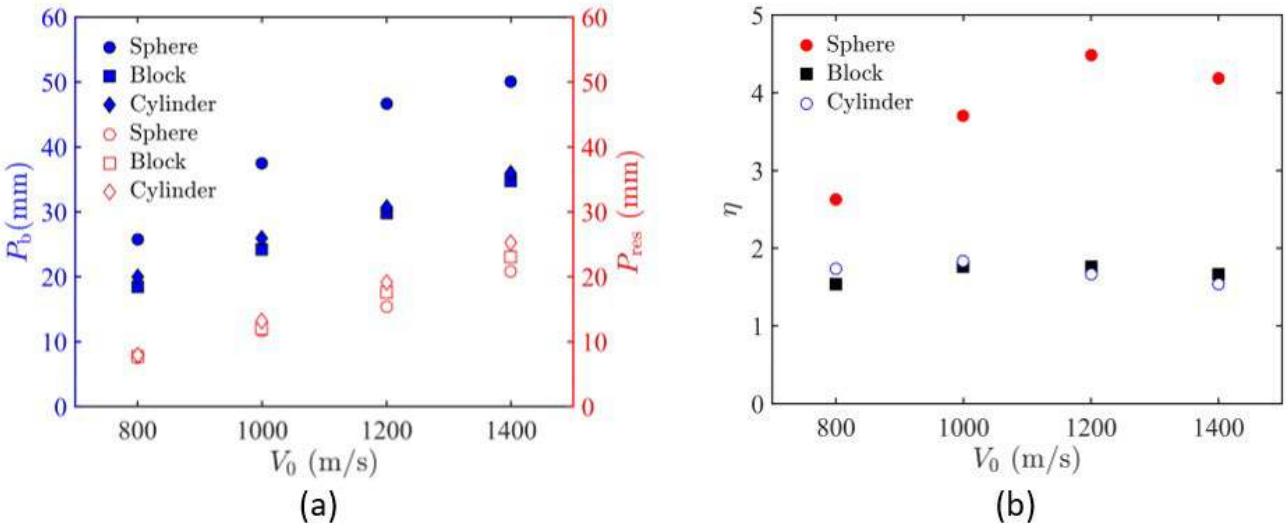


Figure 19 Numerical simulation results of fragment penetration into different targets: (a) Penetration depths of three types of fragments at different velocities; (b) Protection coefficients of the ceramic against the three types of fragments at different velocities.

Figure 20 presents the numerical simulation results for fragment penetration into 6061-T6 aluminum alloy and SiC/Al composite targets at an impact velocity of 1200 m/s.

Combining ballistic tests and numerical simulations, the penetration resistance of the SiC ceramic against fragments shows: For 6061-T6 aluminum alloy targets, the cubic and cylindrical fragments give similar penetration depths at comparable velocities, while the spherical fragment gives a significantly higher depth. For SiC/Al composite targets, the residual penetration depths of the cubic and cylindrical fragments remain similar, but that of the spherical fragment is markedly lower. Hence, the protection coefficient of the ceramic against the spherical fragment is significantly higher than that against the other two fragment shapes.

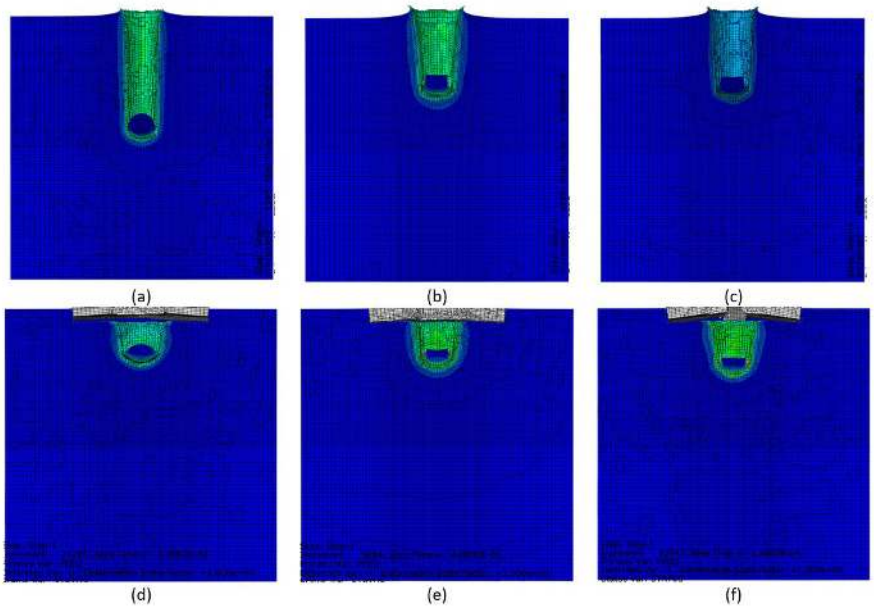


Figure 20 Simulation results of three types of fragments penetrating the two different targets at an impact velocity of 1200 m/s: (a)S-Al; (b)B- Al; (c) C- Al; (d)S-SiC/Al; (e)B-SiC/Al; (f)C-SiC/ Al.

The same trend appears in the simulations, which further reveal a velocity dependence. For SiC/Al composite targets, the residual penetration depths of the three fragments are very close at low velocities but diverge as velocity increases, following the order: cylindrical > cubic > spherical. For 6061-T6 aluminum alloy targets, the spherical fragment always penetrates deeper than the others, while the cylindrical and cubic fragments give similar penetration depths, with the cylindrical slightly deeper than the cubic.

To deeply analyze the behavioral differences of the three types of fragments when penetrating the target, the curves of fragment velocity and acceleration over time were extracted based on the numerical simulation results, as shown in Figure 21.

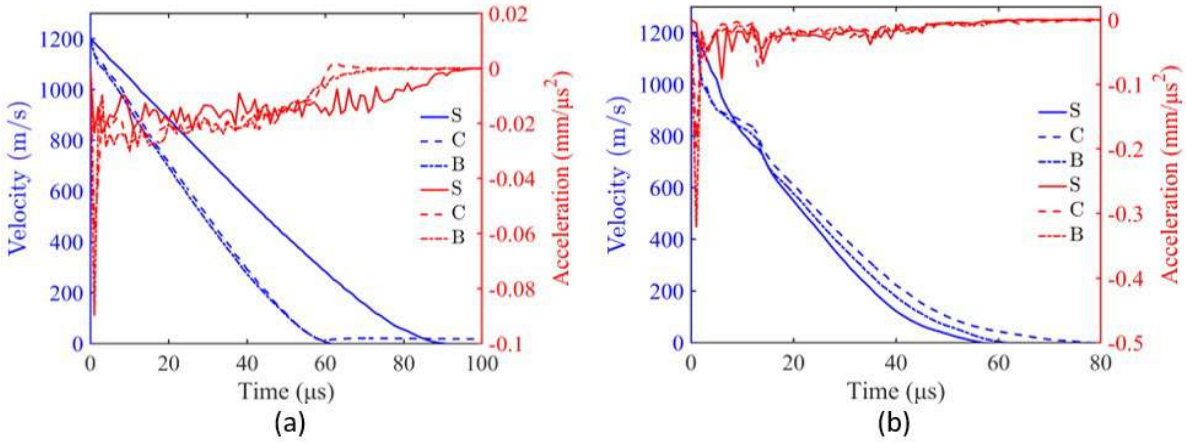


Figure 21 Velocity and acceleration of fragments penetrating SiC/Al composite target over time: (a) 6061-T6 and (b) SiC/Al.

Generally, the penetration process of fragments into an aluminum target can be roughly divided into three stages: cratering, penetration, and plugging. The cratering stage is characterized by the fragment striking the target at its maximum velocity, with impact stress reaching tens of gigapascals (GPa). Both the fragment and the aluminum target undergo severe deformation, and the aluminum target material exhibits plastic flow. As shown in Figure 19(a), when fragments penetrate the aluminum alloy, the velocity of the spherical fragment decreases at a significantly lower rate throughout the entire process compared to the other two shapes. In contrast, the velocity curves of the cylindrical and cubic fragments are similar to each other but markedly different from that of the spherical fragment. At the initial stage of penetration (about 3 μs, corresponding to the cratering stage), the velocities of the cylindrical and cubic fragments decrease much more rapidly. Their acceleration curves exhibit significantly higher peaks, with the cubic fragment showing a higher peak acceleration than the cylindrical one. For the spherical fragment, no distinct acceleration peak is observed at the beginning of penetration, indicating the absence of an obvious cratering stage. During the subsequent penetration stage, the decelerations of the cubic and cylindrical fragments remain close to each other and both are higher than that of the spherical fragment.

When penetrating the SiC/Al composite target (Figure 22(b)), a similar trend is observed within the first 15 μs: the spherical fragment again exhibits a smaller velocity decrease rate compared to the cylindrical and cubic fragments, whose velocities drop much more steeply. However, after 15 μs, the trend reverses. The velocity slope of the spherical fragment becomes steeper than that of the cubic fragment, and the cubic fragment's slope remains steeper than that of the cylindrical fragment. In other words, for times greater than 15 μs, the deceleration order is: spherical > cubic > cylindrical. This indicates that the spherical fragment suffers severe deformation and experiences the highest penetration resistance, while the cylindrical fragment experiences the lowest.

As shown in Figure 22(b), when fragments penetrate the SiC/Al composite target, the velocity of the spherical fragment still decreases relatively smoothly, while the velocities of the cylindrical and cubic fragments decrease much more rapidly within the first 10 μs. This stage corresponds to the initial stage of penetration. When the penetration time reaches 15 μs, the velocity decline trends of the three fragments after penetrating the silicon carbide ceramic tend to converge. To further analyze the plastic deformation of fragments during penetration into ceramics, the head velocity and tail velocity of the fragments were extracted, and the results are shown in Figure 23.

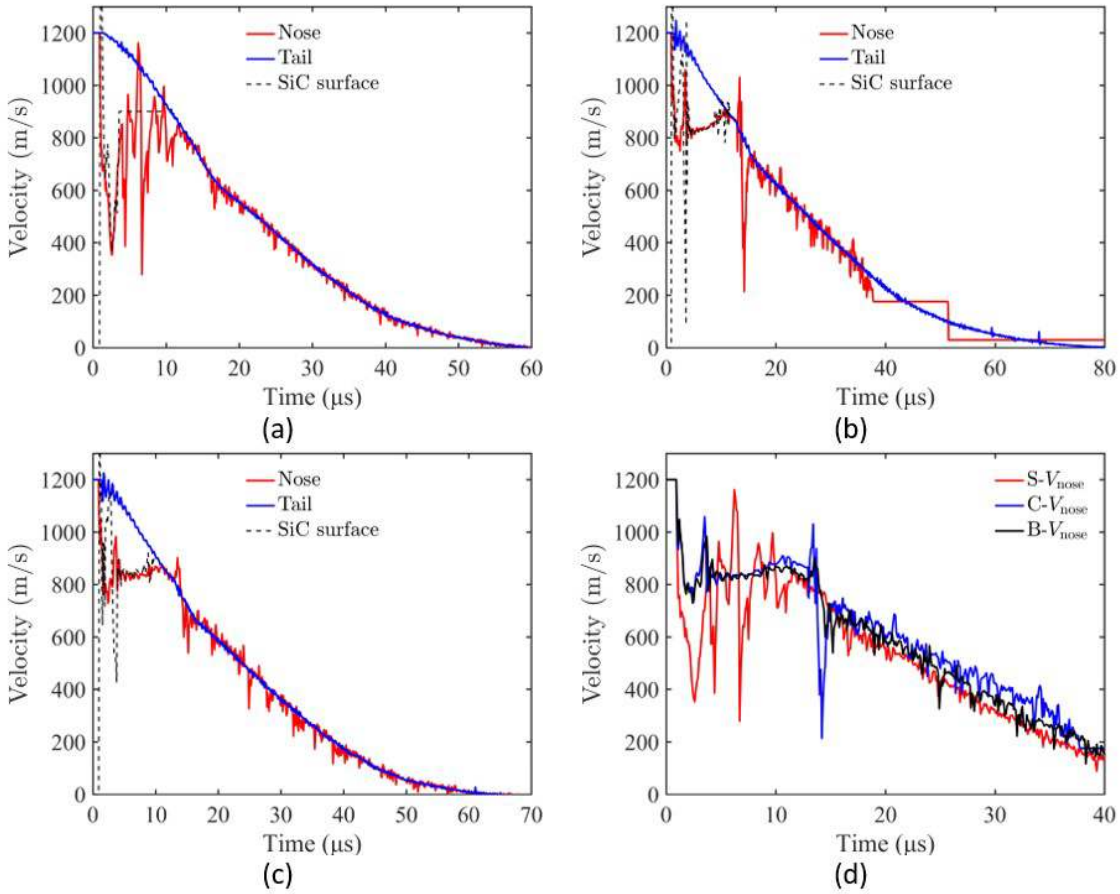


Figure 22 Nose (penetration) and tail velocities versus time for three types of fragments penetrating the SiC/Al composite targets at an impact velocity of 1200 m/s: (a) S-SiCAl; (b) C- SiC/Al; (c) B- SiC/Al; (d) Comparison of nose velocities.

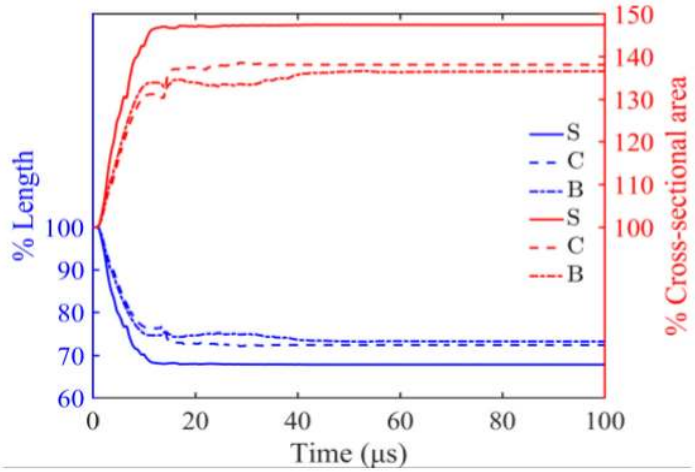


Figure 23 Relative length and relative cross-sectional area of fragments penetrating SiC/Al composite target over time.

Figure 23 shows that the spherical fragment experiences the fastest decrease in length and ends up with the smallest relative length; the relative lengths of the cubic and cylindrical fragments decrease at similar rates, and their final relative lengths are also similar. This result corresponds to the nose-tail velocity difference shown in Figure 22 — the greater the velocity difference, the more significant the change in length. The length change mainly occurs within the first 15 μs of the ceramic penetration stage. The cross-sectional area and length change are negatively correlated. The initial cross-sectional areas are in the order: spherical > cubic > cylindrical, and the ranking of the percentage increase in cross-sectional area is the same, so the order of the final cross-sectional areas remains unchanged. The morphologies of the three fragments after penetrating the two targets are shown in Figure 24.

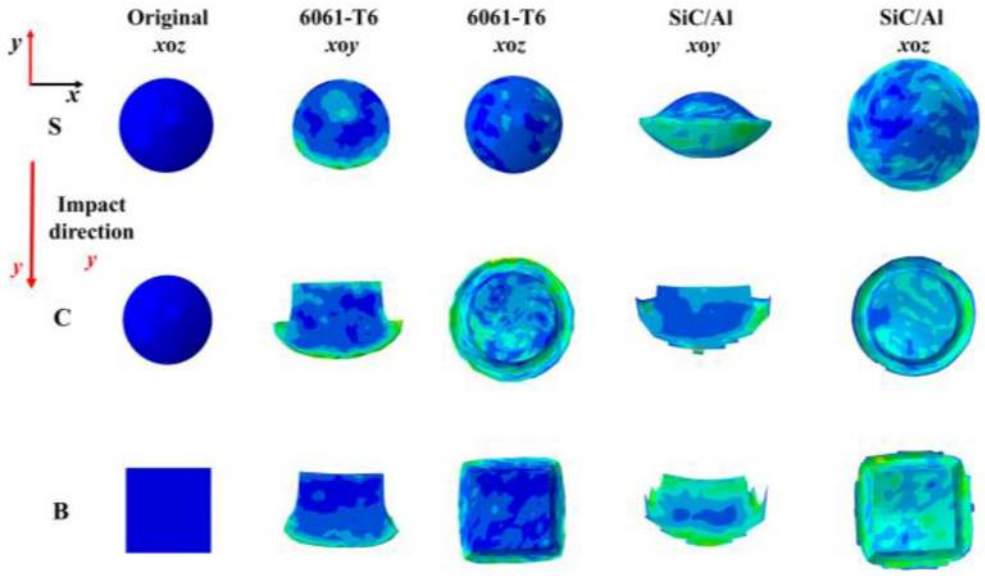


Figure 24 Morphology of three types of fragments penetrating the two different targets at an impact velocity of 1200 m/s.

The mechanism is as follows: When penetrating the 6061-T6 aluminum alloy, the spherical fragment undergoes little deformation and retains its shape advantage, resulting in low penetration resistance and thus a large penetration depth. In contrast, the cubic and cylindrical fragments experience more severe deformation during penetration, leading to a marked increase in cross-sectional area and significantly higher penetration resistance. In addition, more energy is consumed by their deformation process, which further reduces the penetration depth. When penetrating the ceramic composite target, however, the spherical fragment suffers severe deformation, loses its shape advantage, and exhibits the highest penetration resistance among the three fragment shapes. Consequently, the ceramic offers the best protection against spherical fragments, and this advantage becomes more pronounced at higher impact velocities.

5 CONCLUSIONS

In this study, the JH-2 constitutive parameters of SiC ceramic were calibrated through plate impact tests, dynamic and quasi-static uniaxial compression tests. To validate the accuracy of the model parameters, ballistic penetration tests and finite element simulations were conducted. The results of fragment penetration into 6061-T6 aluminum alloy were used to verify the validity of the material parameters for the tungsten alloy and aluminum alloy, while the tests of fragment penetration into SiC/Al composite targets served to validate the correctness of the constitutive parameters for the SiC ceramic. Based on these efforts, the penetration resistance of SiC ceramic against fragments was systematically investigated by combining experiments and numerical simulations. The main conclusions are as follows:

1. Plate impact tests showed that the HEL of the SiC ceramic increased with strain rate, and an average HEL value of 18 GPa was obtained. Dynamic and quasi-static uniaxial compression tests further confirmed that the dynamic compressive strength of the ceramic increased with strain rate, indicating a clear positive strain-rate sensitivity.
2. Comparison of numerical simulations with ballistic tests validated the material parameters for the tungsten alloy and 6061-T6 aluminum alloy. Within the studied impact velocity range, the numerical model predicts fragment penetration depth reasonably well. Simulations of fragment penetration into the SiC/Al composite target agreed well with experiments (error < 9%), confirming the calibrated JH-2 parameters. Penetration process of cubic and cylindrical fragments is sensitive to impact attitude; variations in impact angle significantly affect their penetration resistance and ballistic stability, causing larger simulation-experiment discrepancies. The underlying mechanism of this phenomenon will be one of the focuses of future research.
3. Studies on the penetration resistance of SiC ceramics showed: When penetrating a 6061-T6 aluminum alloy target, cubic and cylindrical fragments also undergo noticeable deformation. However, spherical fragments deform little, and their cross-sectional area becomes smaller than that of the deformed cubic and cylindrical fragments. With less plastic deformation energy dissipation and the benefit of shape factors, spherical fragments exhibit lower penetration resistance, resulting in a significantly greater penetration depth than cubic and cylindrical fragments.

When penetrating SiC/Al composite targets, the above trend reverses. At low velocities, the residual penetration depths of the three fragment shapes are similar; as velocity increases, the differences grow, and the order of residual penetration depth is cylindrical > cubic > spherical. Consequently, the ceramic layer provides a much higher protection coefficient against spherical fragments, and this advantage becomes more pronounced at higher impact velocities.

4. At the initial stage of penetration, the fragment's nose decelerates upon contacting the ceramic, while its tail continues moving forward, creating a significant head-tail velocity difference. This results in a reduction in fragment length and an increase in cross-sectional area. When the fragment completely perforates the ceramic layer, the head-tail velocity difference gradually diminishes, and thereafter the fragment's length and cross-sectional area no longer change. Among the three shapes, the spherical fragment exhibits the largest change in cross-sectional area, which ultimately exceeds that of the cubic and cylindrical fragments. Moreover, the spherical fragment no longer benefits from shape factors. Consequently, its penetration resistance increases sharply, its absolute deceleration becomes higher than that of the other two shapes, and its residual penetration depth ends up being the smallest.

Acknowledgments

The authors would like to acknowledge the National Natural Science Foundation of China (Grant No. 12402468), the China Postdoctoral Science Foundation (Grant No. GZB20250003), and the Shanxi Provincial Basic Research Program (Grant No. 202403021222158).

Author's Contribuitions: Conceptualization, Dacheng Gao; Methodology, Guixiang Yin.; Investigation, Kebin Zhang; Writing - original draft, Dacheng Gao; Writing - review & editing, Dacheng Gao and Wenbin Li; Funding acquisition, Kebin Zhang and Yiming Li; Supervision, Guixiang Yin.

Data availability statement: Research data is only available upon request.

Editor: Rogério José Marczak.

References

Zhai Y X, Wu H, Fang Q. (2020). Interface defeat studies of long-rod projectile impacting on ceramic targets. Defence Technology, 16(1): 50-68.

Sun X, Zhang X, Yan H. (2025). Penetration resistance of ceramic composite structures with a double arrowhead honeycombs interlayer against projectile impact. Ceramics International, 51(9): 11649-11664.

Iqbal M A, Khan M K. (2024). Failure pattern in ceramic metallic target under ballistic impact. Defence Technology, 40(1): 173-190.

Wu Y, Wang X, Ma M, et al. (2023). Research on the anti-penetration behavior and failure mode analysis of different ceramics. Ceramics International, 49(24 Pt. A): 39800-39814.

Yu W H, Li W P, Shangguan Y F, et al. (2023). Relationships between distribution characteristics of ceramic fragments and anti-penetration performance of ceramic composite bulletproof insert plates. Defence Technology, 19(1):103-110.

Feng R, Raiser G F, Gupta Y M. (1998). Material strength and inelastic deformation of silicon carbide under shock wave compression. Journal of Applied Physics, 83(1):79-86.

Holmquist T J, Johnson G R. (2002). Response of silicon carbide to high velocity impact. Journal of Applied Physics, 91(9):5858-5866.

Zhang D, Zhao L, Roy A. (2018). Mechanical behaviour of silicon carbide under static and dynamic compression. Journal of Engineering Materials and Technology, 141(1): 011007.

Gao Y F. (2014). Study on High Strain Rate Deformation of Alumina, Silicon Carbide Ceramics and Al_2O_3/SiC Nanocomposites. Beijing: China University of Geosciences (Beijing).

Rajendran A M. (1994). Modeling the Impact Behavior of AD85 Ceramic Under Multi-Axial Loading. International Journal of Impact Engineering, 15(6): 749-768.

Johnson G R. (1993). An Improved computational constitutive model for brittle materials. High pressure science and Technology, 2.

Simha C H M, Bless S J, Bedford A. (2002). Computational modeling of the penetration response of a high-purity ceramic. International Journal of Impact Engineering, 27(1):65-86.

Ravichandran G, Subhash. (1995). A micromechanical model for high strain rate behavior of ceramics. International Journal of Solids and Structures, 32(17-18):2627-2646.

Espinosa H D. (1995). On the dynamic shear resistance of ceramic composites and its dependence on applied multiaxial deformation. International Journal of Solids & Structures, 32(21):3105-3128.

Espinosa H D, et al. (2005). Micromechanics of Failure Waves in Glass: II, Modeling. Journal of the American Ceramic Society, 80(8):2074-2085.

Steinberg D J. (1992). Computer studies of the dynamic strength of ceramics. Shock Compression of Condensed Matter–, 1992, 01(C3): 447-450.

Johnson G R, Holmquist T J. (1992). A Computational Constitutive Model for Brittle Materials Subjected to Large Strains, High Strain Rates, and High Pressures, Shockwave and High-Strain-Rate Phenomena in Materials, edited by M. A. Meyers, L.E. Murr and K. Staudhammer, Marcel Dekker Inc., New York, 1075-1081.

Quan X, Clegg R A, Cowler M S, et al. (2006). Numerical simulation of long rods impacting silicon carbide targets using JH-1 model. International Journal of Impact Engineering, 33(1/12): 634-644.

Johnson G R, Holmquist T J. (1999). Response of boron carbide subjected to large strains, high strain rates, and high pressures. Journal of Applied Physics, 85(12):8060-8073.

Yin G X, Li W B, Jiang K, et al. (2010). Mechanical properties and high-velocity impact tests of SiCw - reinforced Al2O3-ZrO2 ceramic. Ceramics International, 51(24-PartA): 41547-41562.

Yang Z Q, Pang B J, Wang L W, Chi R Q. (2010). JH-2 model and its application to numerical simulation on Al2O3 ceramic under low-velocity impact. Explosion and Shock Waves, 30(5): 463-471.

Holmquist T J, Templeton D W, Bishnoi K D. (2001). Constitutive modeling of aluminum nitride for large strain, high-strain rate, and high-pressure applications. International journal of impact engineering, 25(3): 211-231.

An R, Wang Y, Fu Q, et al. (2023). Study on parameter acquisition and optimization methods of JH-2 constitutive model for ceramic. International journal of impact engineering, 172: 104424.

An R, Wang Y, Bao J, et al. (2024). Predicting ballistic resistance based on the mechanical properties of armored ceramics. Journal of Materials Research and Technology, 32(000): 2370-2385.

Tang R T, Xu L Y, Wen H M, et al. (2020). A Macroscopic Dynamic Constitutive Model for Ceramic Materials. Chinese Journal of High Pressure Physics, 34(04): 89-99.

Jiang, C., Chen, F., Li, M., & Ma, X. (2001). Penetration and perforation of ceramic/aluminum composite targets by high-speed tungsten alloy sphere. Acta Armamentarii, (01): 37-40.

Li M, Jiang C L, Wang Z C. (2002). A Ballistic Limit Analytical Model of Tungsten Ball Perforating Ceramic/Aluminum Composite Target. Journal of Beijing Institute of Technology (English Edition), 11(4): 389-392.

Mao L, Wang H, Jiang C L, Li M. (2015). Ballistic Limit Velocity of Tungsten Alloy Spherical Fragment Penetrating Ceramic/DFRP Composite Target Plates. Journal of Vibration and Shock, 34(13): 1-5.

Bassett W A, Weathers M S, Wu T C, et al. (1993). Compressibility of SiC up to 68.4 GPa. Journal of Applied Physics, 74(6):3824-3826.

Lahiri S K, Shaw A, Ramachandra L S .On performance of different material models in predicting response of ceramics under high velocity impact. International Journal of Solids and Structures, 176/177.

Wang, J X, Yao Y, Luo C W. (2018). Johnson–Holmquist-II(JH-2) Constitutive Model for Rock Materials: Parameter Determination and Application in Tunnel Smooth Blasting. Applied Sciences, 8(9): 1675.

Grady D E. (1998). Shock-wave compression of brittle solids. Mechanics of Materials, 29(3-4):181-203.

Cook J W H. (1985). Fracture characteristics of three metals subjected to various strains, strain rates, temperatures and pressures. Engineering Fracture Mechanics, 21(1): 31-48.

Holmquist T J, Johnson G R, Grady D E, et al. (1995). High strain rate properties and constitutive Modelling of glass. Glass, 1.

Lundberg P, Renström R, Lundberg B. (2005). Impact of conical tungsten projectiles on flat silicon carbide targets: Transition from interface defeat to penetration. International Journal of Impact Engineering, 2005, 32 (11): 1842-1856.

Robbin J R, Ding J L, Gupta Y M. (2004). Load spreading and penetration resistance of layered structures-a numerical study. International Journal of Impact Engineering, 30(6): 593–615.